applied sciences

MDPI

Article

Research on the Dynamics Model and Jump/Drop Control Strategy of Distributed-Propeller Unmanned Aerial Vehicles

Yansheng Geng [1,2], Xinxin Chen [3], Yinglong He [1,4] and Xiaoping Xu [1,4,*]

[1] School of Aeronautics, Northwestern Polytechnical University, Xi'an 710071, China; ysgeng@hotmail.com (Y.G.); hylong3546@hotmail.com (Y.H.)
[2] The First Aircraft Institute, Aviation Industry Corporation of China Ltd., Xi'an 710089, China
[3] Xi'an ASN Technology Group Co., Ltd., Xi'an 710065, China; cxx.nwpu.edu.cn@mail.nwpu.edu.cn
[4] National Key Laboratory of Aircraft Configuration Design, Xi'an 710072, China
* Correspondence: xuran@nwpu.edu.cn

Abstract: Compared with conventional drones, distributed powered drones have significant advantages in handling stability characteristics, lift and drag characteristics, and takeoff and landing performance. However, there are also challenges such as aerodynamic interference of multi powered slipstream, distributed-power/wing strong-coupling dynamic modeling, and redundant control allocation of distributed-power control mechanisms. The paper has carried out the research on the dynamic modeling method, flight dynamics characteristics analysis, and the design of the control strategy of the jump and steep descent of the distributed dynamic configuration fixed wing unmanned aerial vehicle. A comprehensive aircraft dynamic model considering the influence of propeller slip on aerodynamics was established by combining theoretical derivation with flight experiment data correction. By comparing and analyzing the longitudinal and lateral heading control efficiency of unmanned aerial vehicles under rudder deflection and dynamic differential, a control concept of roll co-ordination control yaw combined with left and right dynamic differential is proposed. Digital simulation and flight tests showed that the established full aircraft dynamics model can accurately reflect the motion laws of distributed-power takeoff and landing unmanned aerial vehicles. The designed takeoff and landing strategy and control scheme can successfully achieve unmanned aerial vehicle takeoff and landing and perform cruising flight tasks.

Keywords: distributed-power unmanned aerial vehicle; dynamic model; distributed slipstream interference; landing and takeoff control strategy; digital simulation; flight test

check for updates

Citation: Geng, Y.; Chen, X.; He, Y.; Xu, X. Research on the Dynamics Model and Jump/Drop Control Strategy of Distributed-Propeller Unmanned Aerial Vehicles. *Appl. Sci.* **2024**, *14*, 12040. https://doi.org/10.3390/app142412040

Academic Editor: Giovanni Bernardini

Received: 9 November 2024
Revised: 11 December 2024
Accepted: 19 December 2024
Published: 23 December 2024

Copyright: © 2024 by the authors. Licensee MDPI, Basel, Switzerland. This article is an open access article distributed under the terms and conditions of the Creative Commons Attribution (CC BY) license (https://creativecommons.org/licenses/by/4.0/).

1. Introduction

Distributed electric propulsion (DEP) technology fully utilizes the size-independent characteristics of a motor system to transform the centralized power layout of conventional aircraft into a distributed propulsion layout according to design requirements. It can achieve an optimal integration of aerodynamics, structure, and power, bringing unprecedented impact to green aviation [1]. With the help of large-scale slip/jet disturbances brought by distributed power, it is expected to greatly improve the aerodynamic performance of aircraft; that is, the suction effect of distributed power can effectively increase the air velocity near the fuselage and, to some extent, suppress the flow of airflow along a spanwise direction [2], resulting in a significant increase in the lift coefficient and lift-to-drag ratio of the aircraft. Many researchers have utilized the efficient lift enhancement effect of distributed electric propulsion systems to develop various types of VSTOL vehicle platform [3–5].

Distributed-power fixed-wing unmanned aerial vehicles have great advantages in terms of their aerodynamic characteristics, takeoff and landing characteristics, environmental friendliness, and flight control robustness. However, due to the coupling between multiple power sources and wing surfaces, research on the flight dynamics and control of this type of unmanned aerial vehicle also faces a series of complex challenges, such as

aerodynamic models considering the influence of distributed-power slipstreams as well as vertical/short takeoff and landing control strategies within the large envelope range.

There are currently two main research methods for modeling the coupled dynamics of power/wing surfaces: theoretical model derivation and engineering test estimation. Robert [6] used the lift line method to simulate interactions between propellers and wings, considering the influence of slip boundaries on lift distribution. However, the accuracy of this method is related to computational complexity, and a large amount of computation is required to obtain accurate results. Waqas Khan et al. [7] established a propeller slipstream model considering the acceleration and slipstream diffusion in a propeller slipstream region using simple analytical derivation and semi-empirical equations and designed measurement experiments to determine the semi-empirical coefficients of the established model. Romain Chiappinelli [8] used the wing segmentation method combined with the assumption of a flat plate to segment a wing according to different inflow conditions. Based on the propeller inflow velocity and control surface deflection angle, the aerodynamic coefficients of each section of the wing were calculated in real time to form a fully maneuverable mechanical model of the influence of propeller slip flow. Lustosa et al. developed a MAVion vertical takeoff and landing unmanned aerial vehicle [9], which combines flow velocity and Slipstream induced velocity as the equivalent airspeed of the drone and introduces a dynamic aerodynamic interaction factor to describe the interaction between the propeller slip and wing surface. Zhao Qingfeng [10] developed a fast calculation method for culvert jet velocity by combining the culvert flow field model and the culvert thrust enhancement coefficient and completed the derivation of a propulsion aerodynamic coupling model based on momentum theory for the presence/absence of dynamic input states. Chen Yongliang [11] used a balance force measurement system to obtain the tension coefficient, height, spacing, and the effect of propeller forward and reverse rotation on the aerodynamic characteristics of a distributed-power layout wing propeller. Wang Chunyang [12] established a coaxial twin-rotor ducted aerodynamic model and a thrust ducted aerodynamic model based on characteristic cross-section calculation using the theory of blade element momentum combined with experimental data and identified the model parameters through experiments. Rao Chong [13] conducted numerical simulations of the low-speed characteristics of a distributed-power unmanned aerial vehicle based on the multiple reference frame (MRF) method and obtained the influence law of the distributed-propeller slip effect on the aerodynamic characteristics of the entire aircraft. However, due to the significant changes in flight speed, angle of attack, flight attitude, and distributed-power rotational speed of distributed-power aircraft in different flight states such as takeoff, landing, transition, and cruise, as well as the existence of nonlinear aerodynamic changes in high-angle-of-attack flight states during takeoff and landing, the dynamic models established in existing research cannot accurately reflect the mechanical characteristics of distributed-power aircraft.

In the field of distributed-power unmanned aerial vehicle takeoff and landing control, scholars at home and abroad have conducted relevant research on control schemes and controller design. Tekinalp [14] conducted a study on control allocation during the transition flight phase of a tilting ducted vertical takeoff and landing unmanned aerial vehicle using the generalized pseudo-inverse method and hybrid pseudo-inverse method. The research results show that the generalized pseudo-inverse method would saturate some control components, while the hybrid pseudo-inverse method could achieve flight stability without causing control saturation. Akici et al. [15] used the PID control method to design control laws for a Lift boosted compound wing UAV in vertical takeoff and landing mode and fixed-wing mode. Cetinsoy et al. [16] designed a hierarchical control system and used the PID control method to design height controllers and attitude controllers for vertical takeoff and landing mode, transition mode, and horizontal mode, respectively. Muraoka et al. [17] selected several state points for controller parameter design based on the different power tilt angles and flap deflection angles during the transition flight process of a tilt powered VTOL UAV. Cook et al. [18] proposed a unified control method for vertical takeoff,

landing, and transition of NASA LA-8 aircraft, which can be used for unified control in all flight states. Raab et al. [19] designed a universal controller based on incremental nonlinear dynamic inversion (INDI) and verified the stability of the controller through vertical takeoff and landing flight tests. Flores et al. [20] proposed a nonlinear control strategy based on nested saturation control and Lyapunov function design for the constant altitude transition flight problem of composite wings with lift thrust.

Li Mao [21] utilized the nonlinear dynamic inverse method to design the control law for a tail-mounted rotary wing aircraft and developed an autonomous landing trajectory planning algorithm and guidance law. Jiang Wen [22] used the classical PID control method and linear quadratic optimal control algorithm to design a pitch angle controller for the vertical takeoff and landing phase of a tiltrotor aircraft. Wu Mei [23] designed a predictive control system using PID and dynamic matrix control algorithms that can effectively track the landing glide trajectory of a flying-wing drone and strictly control the landing glide speed of the drone. Crown Lin [24] established a dual rotor tail sitter unmanned aerial vehicle flight attitude control strategy based on ailerons, total rotor torque, and engine power adjustment. Xiamen University [25] proposed a fixed-wing longitudinal control system based on Total Energy Control (TEC) and applied it to the speed and vertical velocity control of a UAV during vertical takeoff and landing. Wen Jianbo [26] achieved variable configuration VTOL aircraft attitude control through a discrete active disturbance rejection control system consisting of a tracking differentiator, an extended state observer, and state error feedback. Hu Runchang et al. [27] used non-linear dynamic inversion to design the outer-loop control law and L1 adaptive control method to design the inner-loop control law to achieve the control of thrust vectoring takeoff and landing aircraft. Zhong Jingyang [28] used the L1 adaptive control method to study the position control problem during the hovering phase of a tail-mounted vertical takeoff and landing aircraft. Li Yu [29] proposed a longitudinal control law design method for unmanned aerial vehicle landing and takeoff based on L1 adaptive control. It can be seen that current research is mainly focused on the control allocation, control methods, and control strategies for conventional vertical takeoff and landing aircraft, while the control research on the special takeoff and landing mode of distributed-power unmanned aerial vehicles, such as jumping and descending, is not sufficient.

Distributed-power takeoff and landing/vertical takeoff and landing unmanned aerial vehicles have multiple flight stages, including takeoff and landing, vertical takeoff and landing, transition flight, and cruise forward flight. The flight speed, attitude angle, aircraft dynamics characteristics, and control effects of control components undergo significant changes in each flight stage, which poses great challenges to the control scheme and controller design of distributed-power short takeoff and landing/vertical takeoff and landing unmanned aerial vehicles.

Therefore, in response to the problems of strong coupling between distributed-power and wing surfaces, significant aerodynamic effects of propeller slipstreams, and control allocation under redundant distributed-power control mechanisms in distributed-power fixed-wing unmanned aerial vehicles, this paper conducted research on unmanned aerial vehicle dynamics modeling methods, flight dynamics characteristic analysis, and special takeoff and landing control strategy design. Firstly, in response to the problem of poor accuracy of aerodynamic models under the influence of dynamic slip flow, a full aircraft dynamic model considering the influence of distributed-propeller slip flow was established through theoretical derivation combined with flight experiment correction. Secondly, in response to the special jumping and descending flight process of unmanned aerial vehicles, the jumping and descending flight schemes were determined through performance analysis during the climbing phase and performance research during the descending phase. Finally, based on the simulation analysis of the longitudinal and lateral heading control efficiency of the drone, the longitudinal, lateral, and heading control strategies for the drone were determined, and corresponding takeoff and landing control laws were designed. Through full digital simulation and actual flight tests, the unmanned aerial vehicle dynamics model,

characteristics, and takeoff and landing controller were verified to achieve attitude stability and flight safety during the takeoff and landing process of distributed-power aircraft.

2. UAV Dynamics Model

2.1. Drone Layout and Parameters

This paper focuses on a distributed-power tandem wing layout fixed-wing unmanned aerial vehicle (MY-UAV) designed by the research group, as shown in Figure 1. The drone has a flight weight of 9 kg, a front wing span of 2.2 m, a rear wing span of 2.6 m, and a reference area of 1.4 m^2.

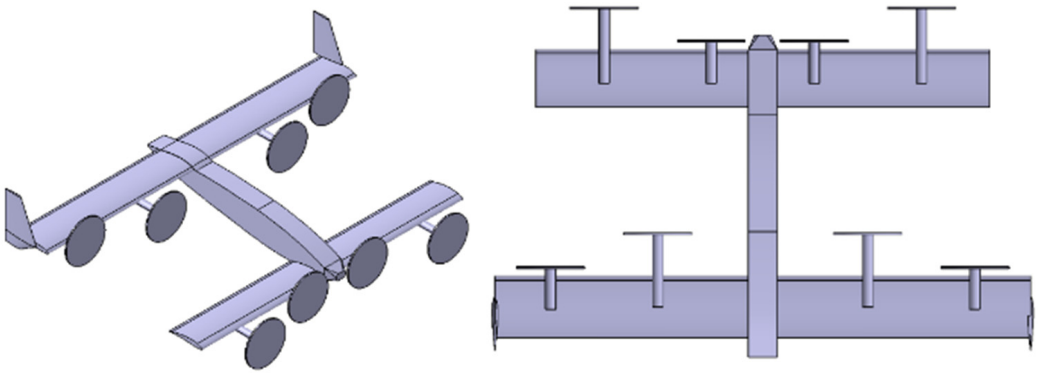


Figure 1. Schematic diagram of MY-UAV layout.

The drone is equipped with eight propellers with a diameter of 13 inches on the front and rear wings. There is one control surface arranged separately at the trailing edge of the wing corresponding to each power propeller. The numbering and grouping of the distributed-power and multiple control surfaces are shown in Figure 2. The power of the eight propellers can be individually controlled, providing not only the necessary pulling force for the drone's flight but also the rotational control torque through throttle differential.

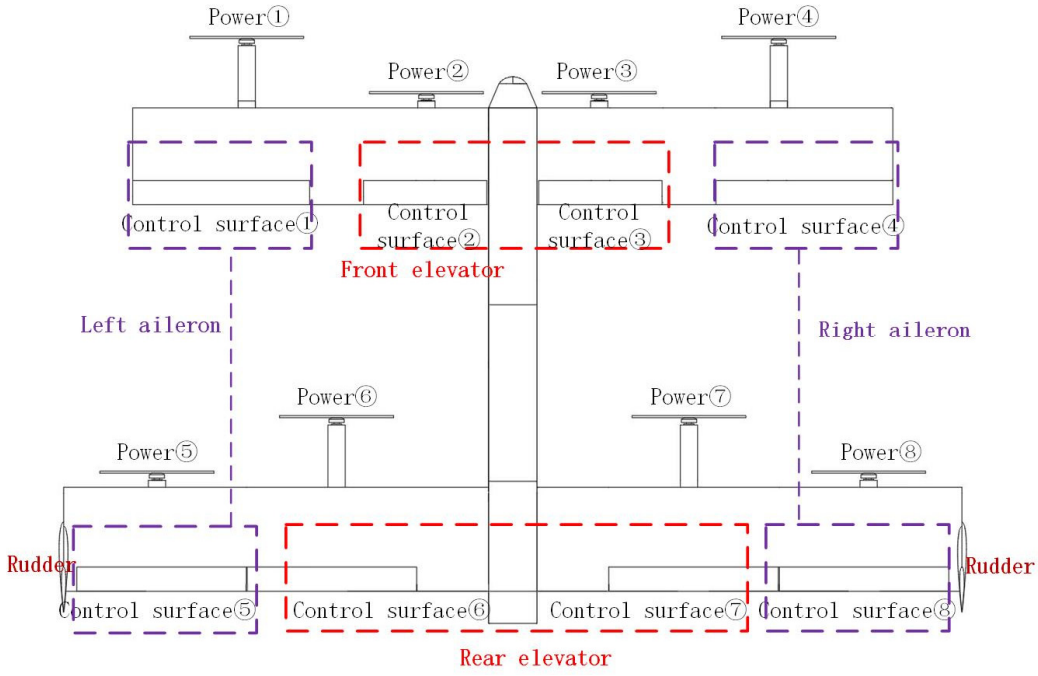


Figure 2. Schematic diagram of MY-UAV distributed-power and multiple control surfaces.

The eight control surfaces are divided into two groups, with two inner front wing surfaces (② ③) and two inner rear wing surfaces (⑥⑦) used as elevators for pitch control; the two outer flaps on the left wing (①⑤) and the two outer flaps on the right wing (④ ⑧) are used as ailerons for roll control. In addition, there is a vertical tail on each side of the rear wing tip, and a rudder is arranged to control the heading. The maximum deflection angle of the designed elevator and aileron is $\pm 40^{\circ}$, and the maximum deflection angle of the rudder is $\pm 25^{\circ}$.

2.2. Aerodynamic Model Considering the Influence of Distributed Slip Flow

MY-UAV adopts a special takeoff and landing method similar to the Neder Drone [3], as shown in Figure 3, with a large stopping angle as the initial state. During the high-angle takeoff and landing process of unmanned aerial vehicles, the free flow velocity is close to zero, and the power demand is relatively high. Therefore, the induced speed of the propeller slipstream is much higher than the free flow velocity, and the aerodynamic force of the wing is mainly generated by the distributed-propeller slipstream. Therefore, the aerodynamic model of unmanned aerial vehicles during takeoff and landing must fully consider the influence of distributed-propeller slipstreams.



Figure 3. Neder Drone takeoff from deck.

(1) Average induced velocity test of propeller slipstreams

In order to accurately obtain the average induced velocity of MY-UAV propeller slipstreams, this paper designed and conducted zero-inflow state propeller slipstream experiments. Due to the fact that the wing profile of the drone can change the incoming flow field and affect the local flow velocity, in order to measure the induced velocity of clean propeller slipstreams at different positions, the inorganic wing measurement method was chosen in this experiment. The experimental system is shown in Figure 4. Firstly, install the selected type of propeller on a fixed platform and connect the testing equipment to control the throttle size of the propeller, while reading information such as voltage, speed, and power. On the other side, install the airspeed tube on a movable platform, with the airspeed tube inlet channel parallel to the propeller shaft. By moving the platform, change the position of the airspeed tube inlet to perform speed measurements at different positions.

According to reference [15], Waqas Khan and Moti Nahon developed and validated a propeller slipstream model for unmanned aerial vehicles in their research, considering the acceleration and diffusion in the propeller slipstream region. The slip velocity of the propeller is relatively small at the center of the propeller shaft. As the distance from the center of the propeller shaft increases, the slip velocity will first increase and then gradually decrease to zero. Considering experimental measurement errors, this article takes the slip velocity at the distance from the center of the propeller shaft as the maximum slip-induced velocity of the section and takes 75% of the maximum slip-induced velocity as the average slip-induced velocity of the section.

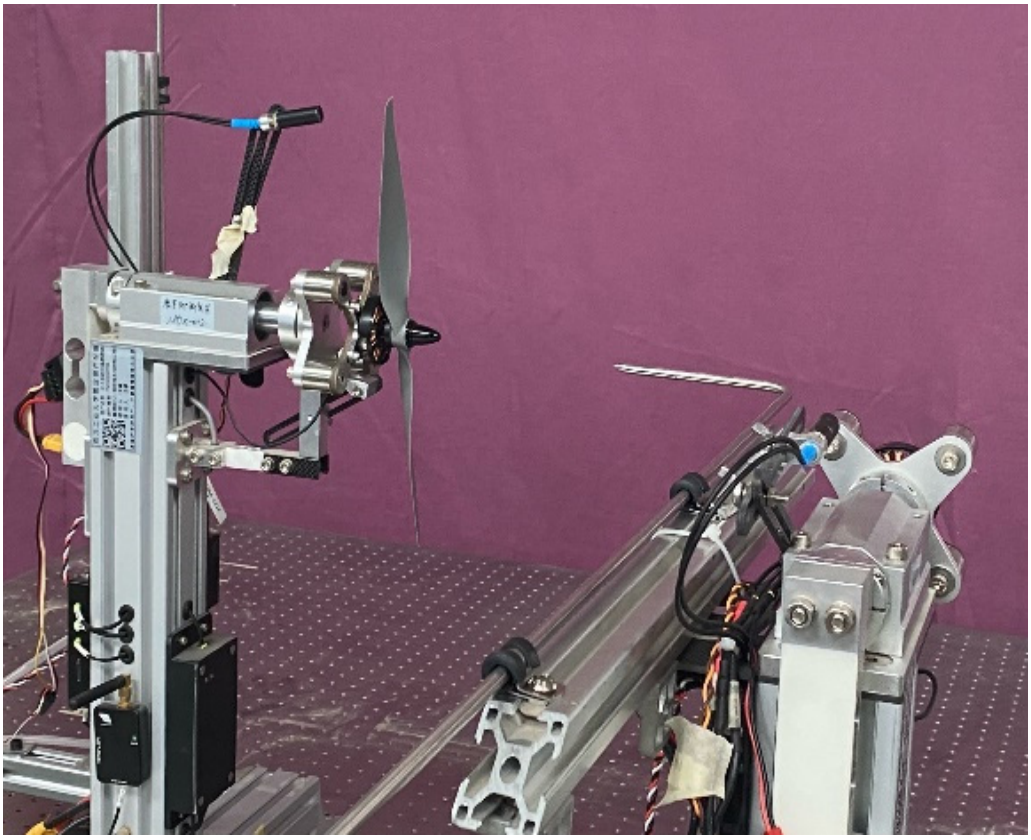


Figure 4. Propeller slip flow velocity test experiment.

Take 75% of the maximum induced slip velocity at the leading edge of the wing as the average induced slip velocity in the slip zone. After interpolation fitting, the variation law of the average induced slip velocity with throttle under zero flow is obtained.

According to reference [15], as the flight speed of the drone increases, the influence of propeller induced slip velocity on the aft closing speed of the drone rotor gradually weakens. Therefore, it is necessary to revise the zero-inflow average induced slip velocity model established in the previous text to expand the application range of the model under different free inflow conditions. After correction, the change curve of the average induced velocity of slipstream with free flow velocity at 1 throttle amount is shown in Figure 5, and the variation curve of the average induced slip velocity with the throttle at different inflow velocities is shown in Figure 6.

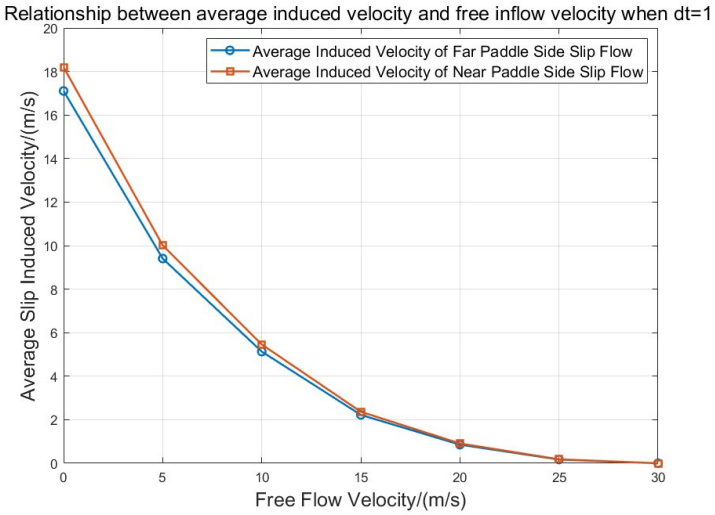


Figure 5. Curve of average induced velocity of slipstream influenced by free flow.

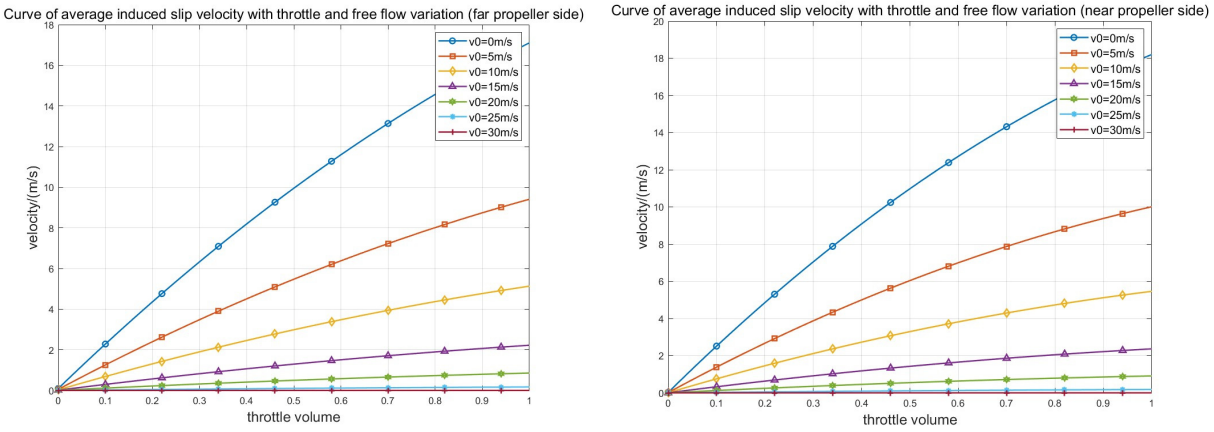


Figure 6. Curve of average induced velocity of different inflow downflow with varying throttle amount.

(2) Experimental study on the mutual influence of multiple propeller slipstreams

To analyze the characteristics of the distributed power propellers affecting each other, two sets of propeller slipstream influence experiments were further designed, with velocity test points arranged along the wing span direction. The experimental system design is shown in Figure 7:

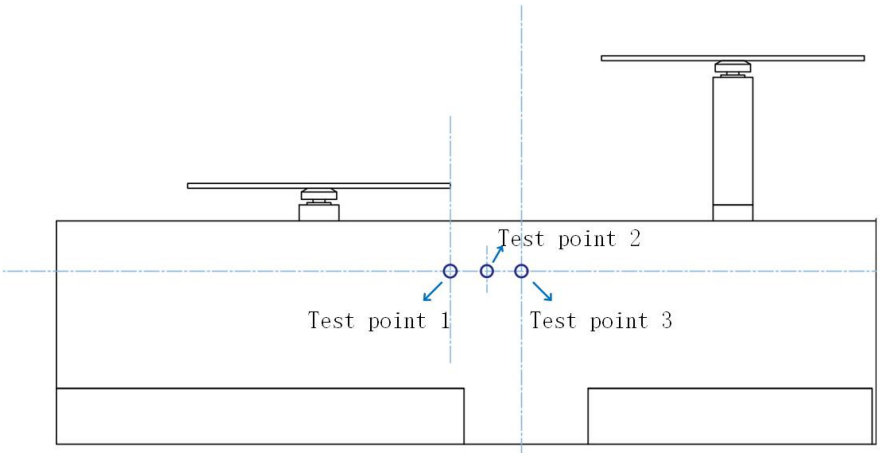


Figure 7. Schematic diagram of experimental test points for analyzing the influence of sliding flow between multiple forces.

According to Figure 7, the slip velocity was tested at three points under different throttle conditions, as shown in Table 1:

Table 1. Experimental test results of sliding flow influence analysis among multiple dynamics.

Throttle	Test Point 1 Slippery Flow Velocity/(m/s)	Test Point 2 Slippery Flow Velocity/(m/s)	Test Point 3 Slippery Flow Velocity/(m/s)
0.25	1.8	0	0
0.5	2.2	1.3	0
0.75	3.3	2	0
1	2.7	1.3	0

From the experimental data and the table above, it can be seen that the slip velocity at test point 3 is 0 m/s under different throttle conditions, indicating that the slip velocities of adjacent propellers will not affect each other. Furthermore, it can be inferred that the slip flow tubes of adjacent propellers do not overlap. Therefore, firstly, independent research is conducted on the slipstream tube and slipstream induced velocity of a single propeller, analyzing the influence of propeller slipstreams on the aerodynamic force and torque of the unmanned aerial vehicle. Then, the impact of distributed-power on the slipstream of each propeller is linearly superimposed to obtain a propeller slipstream influence model.

According to reference [7], the propeller slipstream pipe will first contract and then expand with the increase in the distance between it and the propeller disc plane, while the slipstream velocity will first increase and then decrease, as shown in Figure 8:

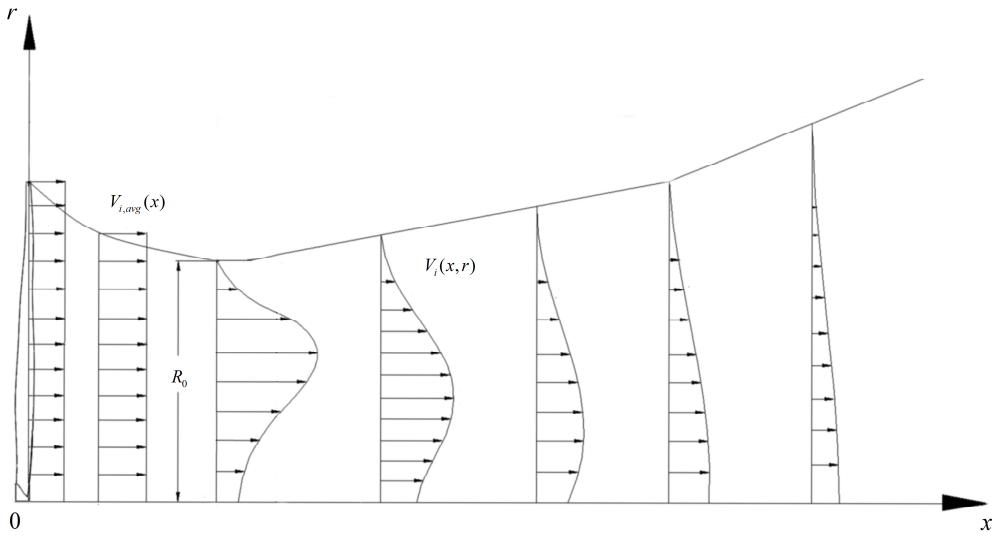


Figure 8. Propeller slip flow tube [15].

To simplify the modeling, combined with the variation laws of the slipstream tube and slipstream velocity, this paper assumes that the effects of slipstream tube expansion and slipstream velocity reduction on the aerodynamic force of the unmanned aerial vehicle can cancel each other out. The velocity at the leading edge of the wing is taken as the average slipstream-induced velocity, and the radius of the propeller disk is taken as the radius of the slipstream tube, and both do not change with position. The distributed-propeller slipstream tube and corresponding slipstream-induced velocity of the unmanned aerial vehicle are shown in Figure 9:

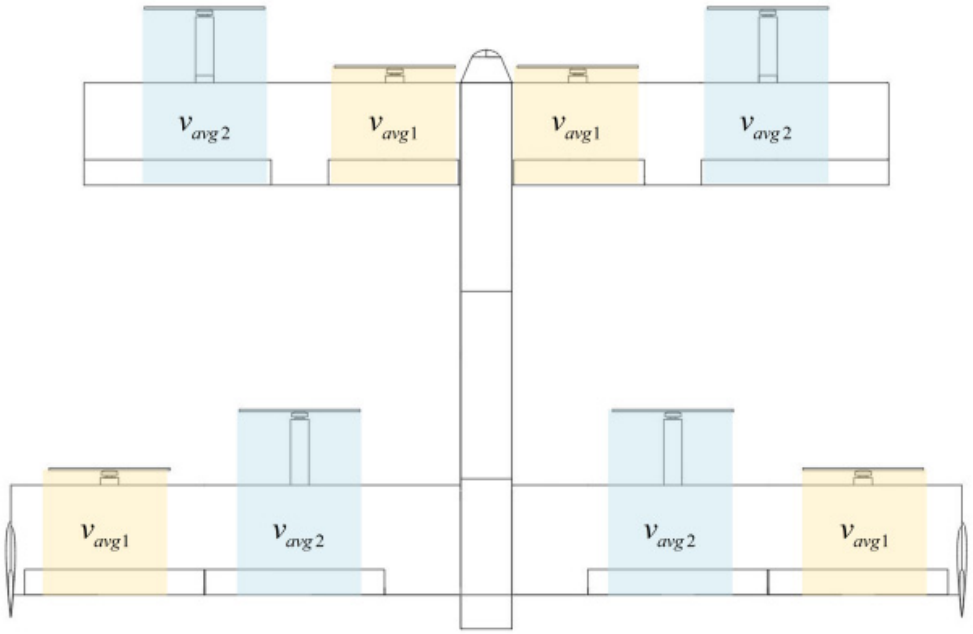


Figure 9. Distributed-power slipstream pipe and average induced velocity.

In Figure 9, the yellow area is the near propeller side propeller slipstream pipe, and the average induced velocity of slipstream in the flow pipe is v_{avg1}. The blue far propeller side propeller slipstream pipe, and the average induced velocity of slipstream in the flow pipe is v_{avg2}.

The diameter of a single propeller slipstream tube is expressed as $D_{slip} = D_p$, the propeller slipstream tube area is expressed as $S_{slip} = D_{slip} \cdot \bar{c}$, and the average induced velocities of the inner and outer propeller slipstream are expressed as v_{avg1}, v_{avg2}, respectively. Considering the forward free flow of the drone, the combined velocity of the slip zone is the vector sum of the average slip-induced velocity and the free flow velocity, and the equivalent angle of attack of the slip zone is the angle between the combined velocity of the slip zone and the axis direction of the aircraft, as shown in Figure 10:

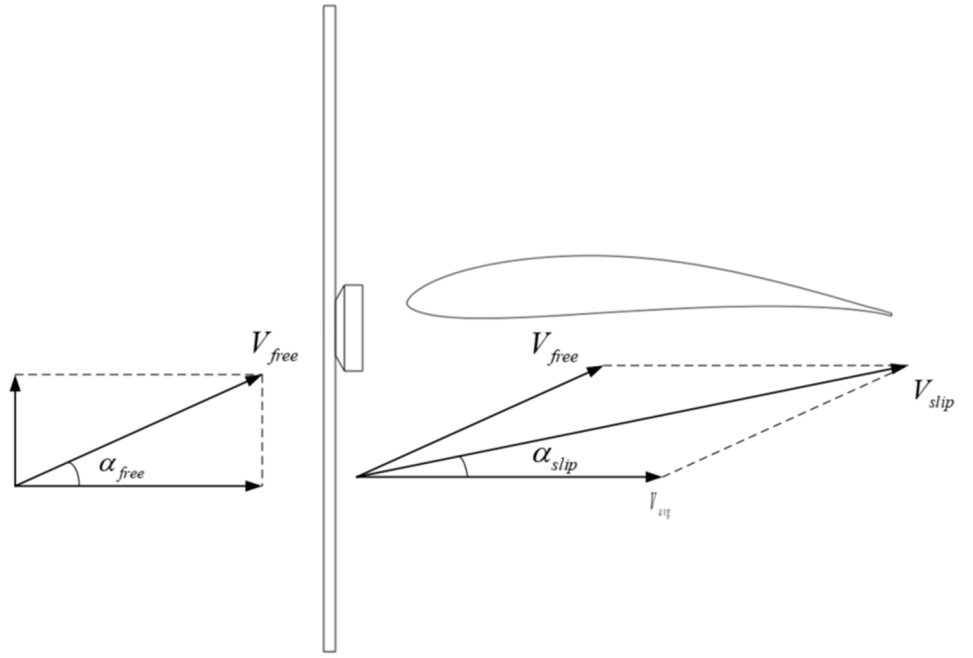


Figure 10. Schematic diagram of combined velocity in the slip zone.

The derivation of the combined velocity V_{slip} and equivalent angle of attack α_{slip} in the slip zone is as follows:

$$\vec{V}_{slip} = \vec{V}_{free} + \vec{V}_{avg} \tag{1}$$

$$V_{slip} = \sqrt{V_{free}^2 + V_{avg}^2 - 2V_{free} \cdot V_{avg} \cdot \cos(\pi - \alpha_{free})} \tag{2}$$

$$\alpha_{slip} = \arcsin \frac{V_{free} \cdot \sin \alpha_{free}}{V_{slip}} \tag{3}$$

where α_{free} is the angle of attack of the free flow, namely the angle between the free flow and the x-axis direction of the aircraft.

(3) Consider the aerodynamic model of slip flow

Under the influence of distributed-power propellers, the wings and control surfaces of unmanned aerial vehicles can be divided into the slip flow influence zone and the free flow zone. The influence of slip flow on the aerodynamic force of the aircraft is mainly reflected in the changes in local dynamic pressure and angle of attack on the wings. This paper divides the unmanned aerial vehicle into a free flow zone and eight slip flow zones and analyzes and models the aerodynamic force and aerodynamic torque separately, as shown in Figure 11.

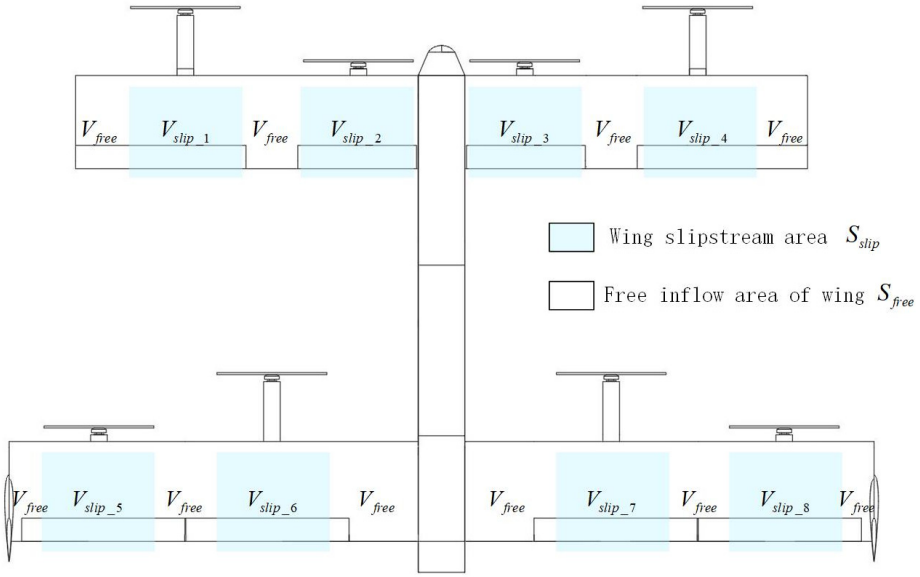


Figure 11. MY-UAV wing segmented aerodynamic modeling method considering slip flow.

To simplify modeling, this article assumes that all free flow areas of the entire machine have consistent dynamic pressure and airflow angle. The aerodynamic coefficient within the free flow area can be expressed as follows:

$$\begin{cases} C_{D_free} = C_{D0} + C_D^{\alpha}\alpha_{free} + \mathrm{k} \cdot {\alpha_{free}}^2 + \sum\limits_{i=1}^{8} (C_D^{\delta_{ea_i}} \cdot \delta_{ea_i}) + C_D^{\delta_r} \cdot \delta_r \\ C_{Y_free} = C_Y^{\beta}\beta + \mathrm{m}_1\beta^2 + \mathrm{m}_2\beta^3 + \sum\limits_{i=1}^{8} (C_Y^{\delta_{ea_i}} \cdot \delta_{ea_i}) + C_Y^{\delta_r} \cdot \delta_r + C_Y^{p}\overline{p} + C_Y^{r}\overline{r} \\ C_{L_free} = C_{L0} + C_L^{\alpha}\alpha_{free} + \mathrm{k}_1 \cdot {\alpha_{free}}^2 + \mathrm{k}_2 \cdot {\alpha_{free}}^3 + \sum\limits_{i=1}^{8} (C_L^{\delta_{ea_i}} \cdot \delta_{ea_i}) + C_L^{q}\overline{q} \end{cases} \tag{4}$$

The propeller slip effect of unmanned aerial vehicles is mainly reflected in the changes in local dynamic pressure and airflow angle on the wings. Therefore, in order to simplify modeling and facilitate the construction of dynamic simulation models, it can be considered that the influence of propeller slip on the aerodynamic parameters of unmanned aerial

vehicles can be ignored, and only the dynamic pressure and local angle of attack can be changed. The aerodynamic coefficient of the first slip zone can be expressed as follows:

$$\begin{cases} C_{D_slip_i} = C_{D0} + C_D^{\alpha}\alpha_{slip} + \mathrm{k}\cdot {\alpha_{slip}}^2 + C_D^{\delta_{ea_i}}\cdot\delta_{ea_i} + C_D^{\delta_r}\cdot\delta_r \\ C_{Y_slip_i} = C_Y^{\beta}\beta + \mathrm{m}_1\beta^2 + \mathrm{m}_2\beta^3 + C_Y^{\delta_{ea_i}}\cdot\delta_{ea_i} + C_Y^{\delta r}\cdot\delta_r + C_Y^{p}\overline{p} + C_Y^{r}\overline{r} \\ C_{L_slip_i} = C_{L0} + C_L^{\alpha}\alpha_{slip} + \mathrm{k}_1\cdot {\alpha_{slip}}^2 + \mathrm{k}_2\cdot {\alpha_{slip}}^3 + C_L^{\delta_{ea_i}}\cdot\delta_{ea_i} + C_L^{q}\overline{q} \end{cases} \tag{5}$$

The three-axis resultant force of the drone is expressed as follows:

$$\begin{aligned} F_A &= F_{free} + F_{slip} \\ &= \begin{bmatrix} \frac{1}{2}C_{D_free}\rho V_{free}^2 S_{free} + \sum_{i=1}^{8}\left(\frac{1}{2}C_{D_slip_i}\rho V_{slip_i}^2\cdot\frac{1}{8}S_{slip}\right) \\ \frac{1}{2}C_{Y_free}\rho V_{free}^2 S_{free} + \sum_{i=1}^{8}\left(\frac{1}{2}C_{Y_slip_i}\rho V_{slip_i}^2\cdot\frac{1}{8}S_{slip}\right) \\ \frac{1}{2}C_{L_free}\rho V_{free}^2 S_{free} + \sum_{i=1}^{8}\left(\frac{1}{2}C_{L_slip_i}\rho V_{slip_i}^2\cdot\frac{1}{8}S_{slip}\right) \end{bmatrix} \end{aligned} \tag{6}$$

Similarly, the pitch moment of the entire drone is expressed as follows:

$$m_{free} = \frac{1}{2}C_{m_free_no\delta_e}\rho V_{free}^2 S_{free}\bar{c} + \frac{1}{2}C_{m_free_\delta_e}\rho V_{free}^2\left(S_{free}+S_{slip}\right)\bar{c} \tag{7}$$

$$\begin{aligned} m_{slip} &= \sum_{i=1}^{8}\left(\frac{1}{2}C_{m_slip_i_no\delta_e}\rho V_{slip_i}^2\frac{1}{8}S_{slip}\bar{c}\right) \\ &+ \sum_{i=1}^{8}\left[\frac{1}{2}C_{m_slip_i_\delta_e}\rho V_{slip_i}^2\left(S_{free}+S_{slip}\right)\bar{c}\right] \end{aligned} \tag{8}$$

$$m_A = m_{free} + m_{slip} \tag{9}$$

For the lateral roll moment and yaw moment, first calculate the lateral yaw moment coefficient of the entire aircraft without slip flow:

$$C_l = C_l^{\beta}\beta + \sum_{i=1}^{8}\left(C_l^{\delta_{ea_i}}\cdot\delta_{ea_i}\right) + C_l^{\delta_r}\delta_r + C_l^{p}\overline{p} + C_l^{r}\overline{r} \tag{10}$$

$$C_n = C_n^{\beta}\beta + \sum_{i=1}^{8}\left(C_n^{\delta_{ea_i}}\cdot\delta_{ea_i}\right) + C_n^{\delta_r}\delta_r + C_n^{p}\overline{p} + C_n^{r}\overline{r} \tag{11}$$

Calculate the lateral yaw moment generated by the aerodynamic force increment in the unmanned aerial vehicle in each slip zone:

$$\begin{aligned} \Delta l_{slip_i} &= \Delta L_{slip_i}\cdot y_{slip_i} \\ \Delta n_{slip_i} &= \Delta D_{slip_i}\cdot y_{slip_i} \end{aligned} \tag{12}$$

Among them, y_{slip_i} is the x-axial distance between the aerodynamic center of each slip zone and the aerodynamic center of the whole machine.

The lateral heading torque of the drone is obtained as follows:

$$\begin{aligned} l_A &= \frac{1}{2}C_l\rho V_{free}^2(S_{free}+S_{slip})b + \sum_{i=1}^{8}\Delta l_{slip_i} \\ n_A &= \frac{1}{2}C_n\rho V_{free}^2(S_{free}+S_{slip})b + \sum_{i=1}^{8}\Delta n_{slip_i} \end{aligned} \tag{13}$$

The aerodynamic force and torque derivation of unmanned aerial vehicles considering slip flow have been completed above.

Obtain the scalar equations for the dynamics of the center of mass of the body axis system:

$$\begin{cases} m(\frac{du}{dt} + qw - rv) = \sum_{i=1}^{8}(T_i \cos\theta_{tdi}) - D\cos\alpha\cos\beta \\ -Y\cos\alpha\sin\beta + L\sin\alpha - mg\sin\theta \\ m(\frac{dv}{dt} + ru - pw) = -D\sin\beta + Y\cos\beta + mg\sin\phi\cos\theta \\ m(\frac{dw}{dt} + pv - qu) = -\sum_{i=1}^{8}(T_i \sin\theta_{tdi}) - D\sin\alpha\cos\beta \\ -Y\sin\alpha\sin\beta - L\cos\alpha + mg\cos\phi\cos\theta \end{cases} \tag{14}$$

The scalar equation system for the rotational dynamics of the body axis around the center of mass is as follows:

$$\begin{cases} I_x\frac{dp}{dt} + (I_z - I_y)qr - I_{zx}(pq + \frac{dr}{dt}) = l + \sum_{i=1}^{8} Q_{xi} + \sum_{i=1}^{8} l_{Ti} \\ I_y\frac{dq}{dt} + (I_x - I_z)rp + I_{zx}(p^2 - r^2) = m + \sum_{i=1}^{8} Q_{yi} + \sum_{i=1}^{8} m_{Ti} \\ I_z\frac{dr}{dt} + (I_y - I_x)pq + I_{zx}(qr - \frac{dp}{dt}) = n + \sum_{i=1}^{8} Q_{zi} + \sum_{i=1}^{8} n_{Ti} \end{cases} \tag{15}$$

Among them, Q_{xi}, Q_{yi}, and Q_{zi} are related to aerodynamic moments or torques acting on the UAV. These terms contribute to the overall rotational motion of the UAV around its center of mass.

2.3. Dynamic Model Correction and Verification Based on Flight Tests

The aerodynamic model modeling research and propeller slip influence experiment conducted in the previous section were carried out under zero free flow conditions. Although the parameter changes in the power at high speeds and the induced velocity of propeller slip under incoming flow conditions were extrapolated and corrected during the modeling process, the accuracy of the established model had not been verified yet.

Therefore, this paper further designed the MY-UAV flight test and combined the flight test data to revise and verify the established aerodynamic and dynamic models. The designed drone flight test mainly includes three flight projects: normal taxiing takeoff, high-speed cruising, and low-speed large-angle climbing. Figure 12 shows the process of the MY-UAV drone flight experiment.



(**a**) (**b**)

Figure 12. Flight experiment process picture of MY-UAV: (**a**) rolling takeoff process; (**b**) low-speed and high-angle climb process in the air.

In this flight experiment, the drone was powered by three sets of 6S batteries in parallel and equipped with an eagle power sensor for power acquisition. An unmanned aerial vehicle dynamics model was built using Matlab/Simulink, and the simulation results of the cruise process were compared with actual flight experiment data.

The digital simulation results of the cruise section are shown in Figure 13:

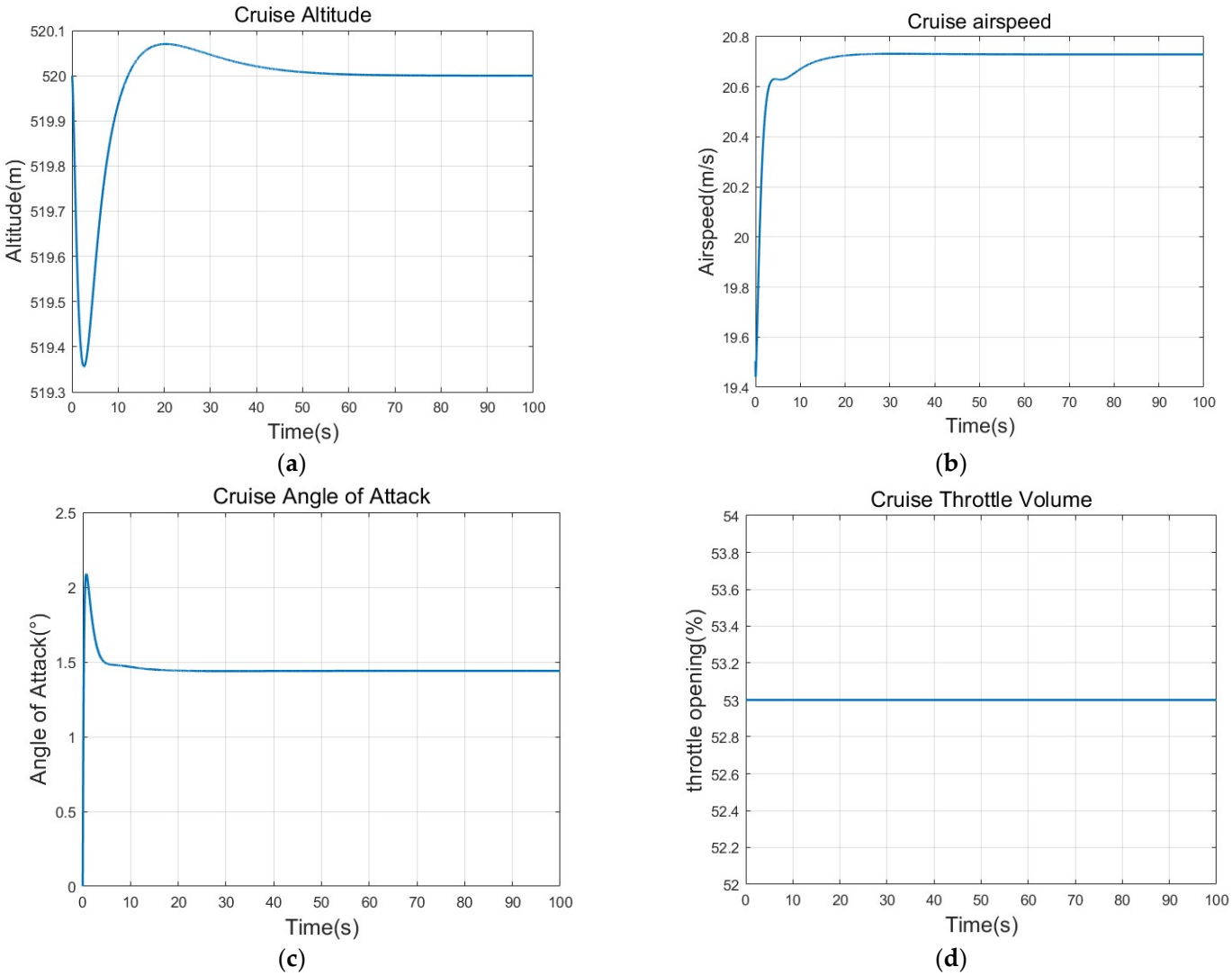


Figure 13. Digital simulation results of cruise segment. (**a**) Cruise segment simulation—altitude; (**b**) cruise segment simulation—airspeed; (**c**) cruise segment simulation—angle of attack; (**d**) cruise segment simulation—throttle amount.

The simulation results show that the drone can fly at a constant altitude at 53% throttle opening, maintaining an angle of attack of 1.4°, and an airspeed of 20.73 m/s, in good agreement with experimental flight data.

To further verify the accuracy of the modified dynamic model, it was reapplied to the digital simulation experiment for taxiing takeoff. The simulation results are shown in Figure 14:

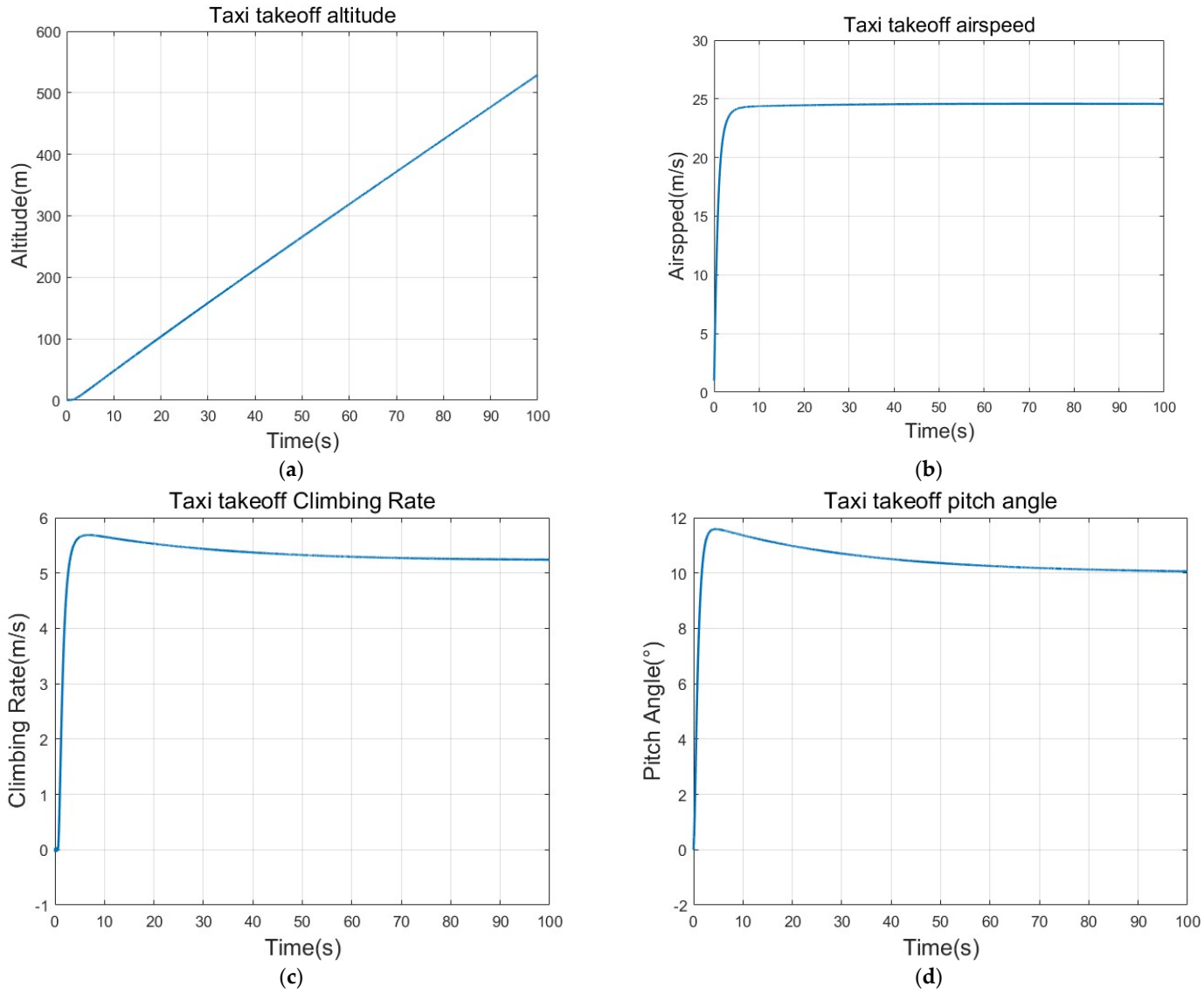


Figure 14. Digital simulation results of takeoff climb phase. (**a**) Taxiing takeoff simulation—altitude; (**b**) taxiing takeoff simulation—airspeed; (**c**) taxiing takeoff simulation—climb rate; (**d**) taxiing takeoff simulation—pitch angle.

The simulation results show that after taxiing off the ground, the drone can steadily climb at an airspeed of about 24.6 m/s, a climb rate of 5.3 m/s, and a pitch angle of 10.2°, with a climb height of about 48 m within 10 s.

After extracting data from the actual flight experiment of the drone during the taxiing and takeoff phase, as shown in Figure 15, it can be observed that the drone can steadily climb at an airspeed of approximately 25 m/s, a climb rate of 4.1 m/s, and a pitch angle of 10° after taxiing off the ground, with a climb height of approximately 43 m within 10 s.

The results of the MY-UAV flight tests were compared and analyzed with the simulation results. The results indicate that the airspeed error during the stable climb phase of the MY-UAV does not exceed 4%, the climb rate error does not exceed 20%, and the pitch angle error does not exceed 7%. It can be seen that through the correction method of the above dynamic model, it can effectively ensure that the dynamic model has good agreement with the actual flight characteristics of the unmanned aerial vehicle, which further indicates that the established dynamic model has high reference value for subsequent takeoff and landing control of MY-UAV.

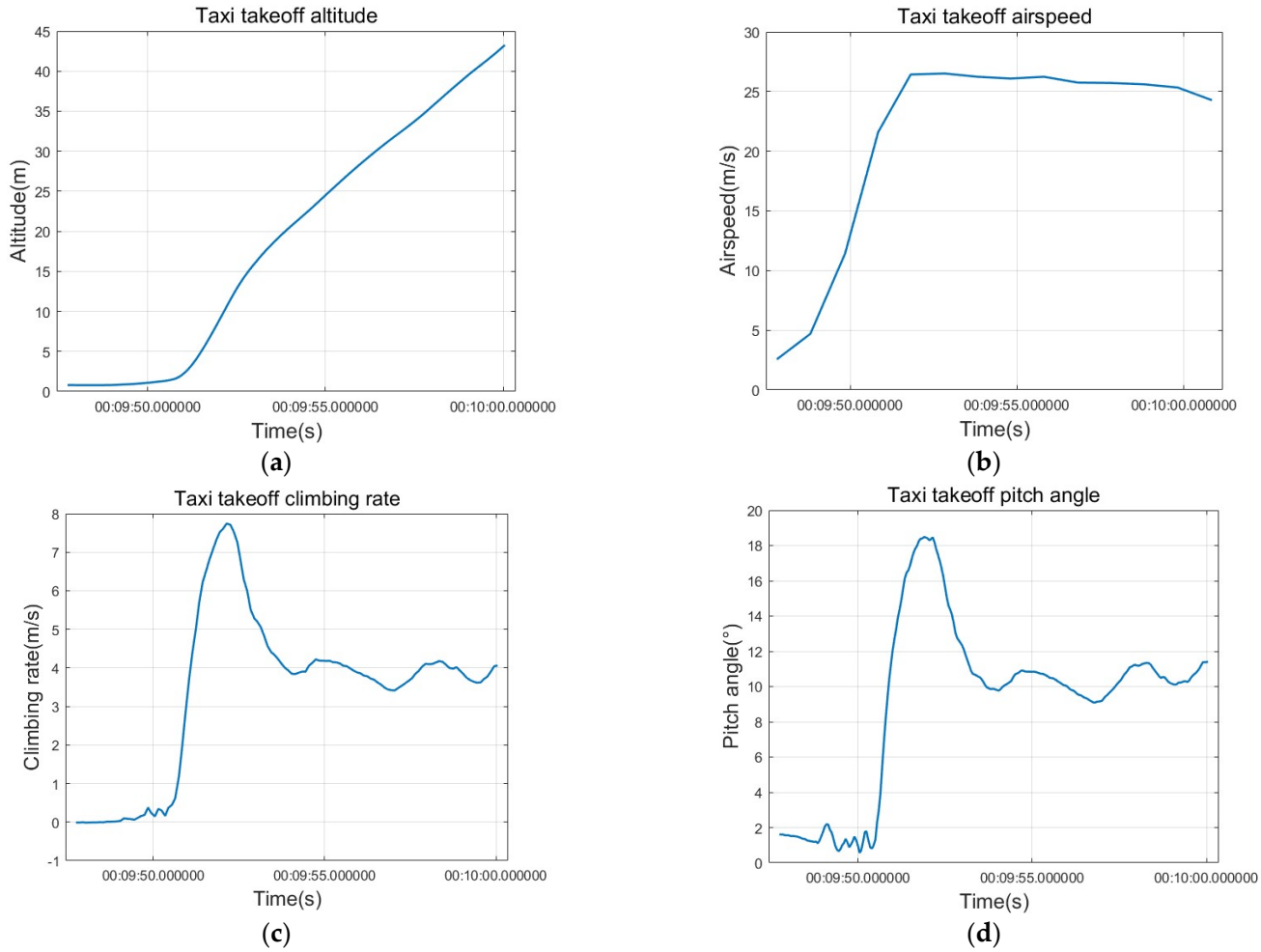


Figure 15. Real flight data during takeoff climb phase. (**a**) Taxiing takeoff actual flight—altitude; (**b**) taxiing takeoff actual flight—airspeed; (**c**) taxiing takeoff actual flight—climb rate; (**d**) taxiing takeoff actual flight—pitch angle.

3. Performance Analysis and Control Strategy Design of Unmanned Aerial Vehicles During Rapid Ascent and Descent

To meet the requirements of special mission scenarios, MY-UAV drones choose takeoff and landing methods of jumping and steep slope descent. To explore the jumping and steep descent capabilities of drones, it is necessary to analyze their basic aerodynamic characteristics, stability, and maneuverability, evaluate their climb and glide performance, and determine the flight envelope for large-angle climbing and large-angle gliding of drones. Further combining the constraints of drone configuration, aerodynamic characteristics, and mission scenarios, the total energy consumption, rudder control margin, vertical velocity, and other indicators of different climb and glide schemes are analyzed and compared, and ultimately, the optimal drone takeoff and landing control strategy is obtained.

3.1. Climbing Performance Analysis and Leap Control Strategy Design

To meet the requirements of the mission scenario, the MY-UAV drone chooses to complete the takeoff mission by jumping up at a large stopping angle. The entire takeoff process of the drone will be divided into two stages: jumping acceleration and stable climbing. The acceleration process of the drone jumping up will be designed to achieve the fastest acceleration with the maximum throttle, which accounts for a very small proportion of the entire takeoff mission time. Therefore, the focus of the jumping up process is to find the most favorable climbing flight state.

(1) Performance Analysis of UAV Climbing

In order to seek a better strategy for unmanned aerial vehicle jumping and climbing, the force during the climbing process of the distributed-propeller fixed-wing unmanned aerial vehicle is first analyzed. Figure 16 is a schematic diagram of the force during the climbing state of the unmanned aerial vehicle.

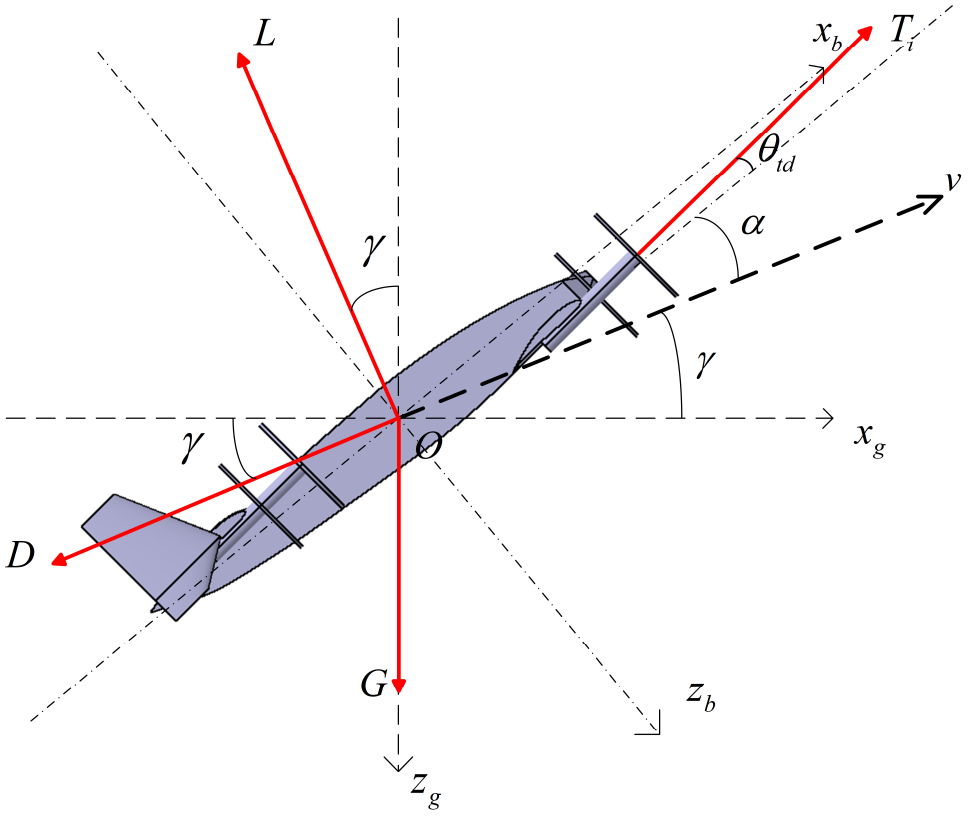


Figure 16. Force diagram of MY-UAV drone climbing state.

Without considering wind interference, the drone's flight altitude is set to 500 m, and climb balancing is performed on the drone:

$$\begin{cases} -L\sin\gamma - D\cos\gamma + \\ \sum_{i=1}^{8} T_{xi}\cos(\alpha+\gamma) + \sum_{i=1}^{8} T_{zi}\sin(\alpha+\gamma) = 0 \\ m + \sum_{i=1}^{8} m_{Ti} = 0 \\ -L\cos\gamma + D\sin\gamma - \\ \sum_{i=1}^{8} T_{xi}\sin(\alpha+\gamma) + \sum_{i=1}^{8} T_{zi}\cos(\alpha+\gamma) + G = 0 \end{cases} \tag{16}$$

where $m_{Ti} = T_{xi} \cdot l_{zi} - T_{zi} \cdot l_{xi}$, $T_{xi} = T_i \cos\theta_{td}$, $T_{zi} = -T_i \sin\theta_{td}$.

The relationship between each state quantity, flight speed, and climb angle is obtained as shown in Figure 17:

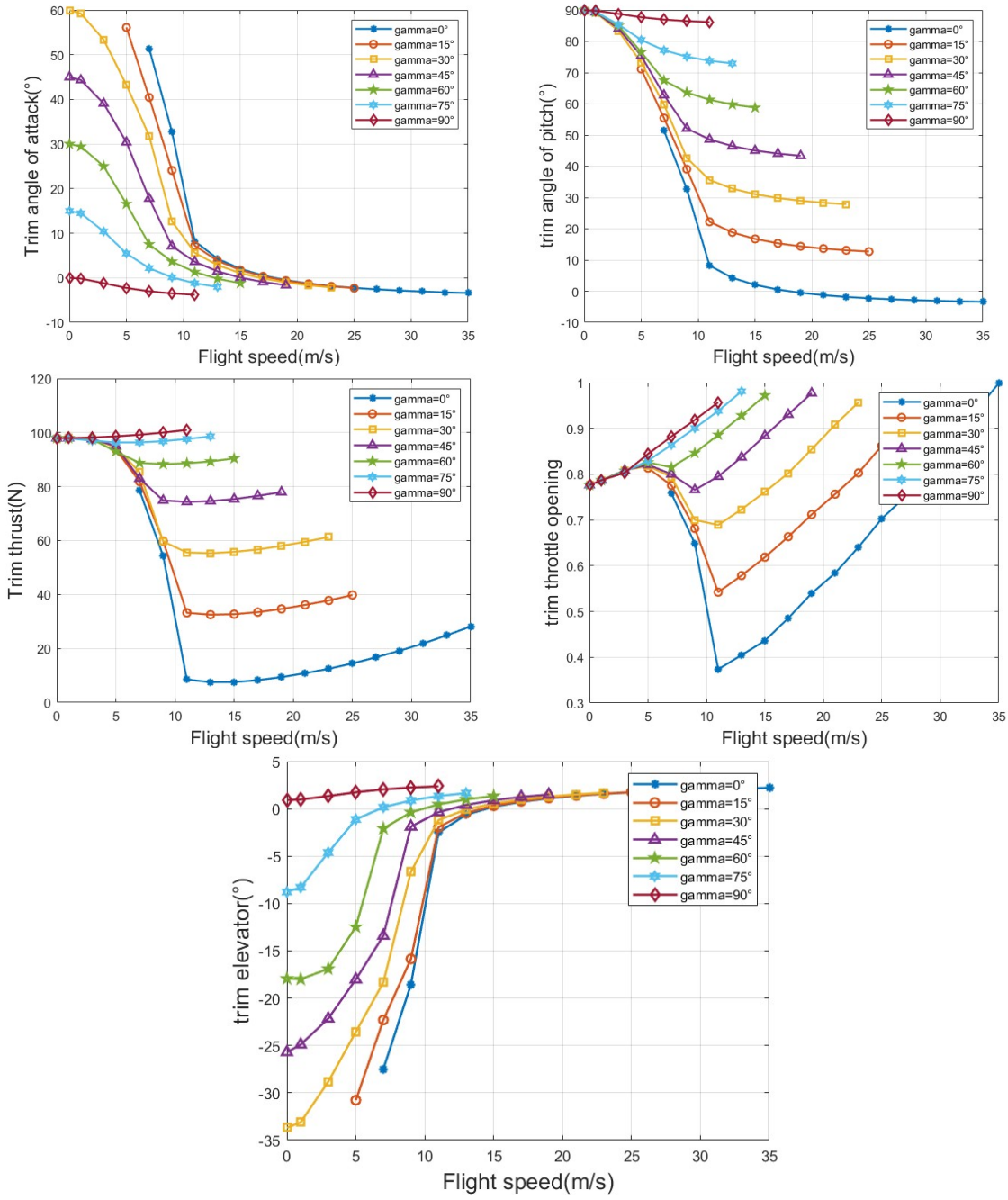


Figure 17. The variation curve of MY-UAV climb trim state variables with flight speed.

By combining the curve of the angle of attack with speed and the curve of the pitch angle with speed, it can be concluded that in order for the drone to meet the requirements of a small climb angle and low-speed climb tasks, it needs to maintain a high-angle-of-attack flight state. At this time, the drone's balance state is very sensitive to changes in flight speed and climb angle, which is not conducive to the stable climb of the drone. When the drone climbs at a larger climb angle or speed, its balance state is relatively sluggish due to changes in flight speed and climb angle, which is beneficial for the stable climb of the drone.

Combining the curve of balancing thrust with speed and the curve of balancing throttle opening with speed, it can be concluded that as the climbing angle of the drone increases, the required thrust and throttle for drone climbing also increase accordingly. As the climbing speed of the drone increases, the required thrust and throttle do not increase

monotonically, and there is a minimum required thrust and minimum required throttle during this process. Therefore, when considering the stable climb of drones, their designed flight speed should be as close as possible to the flight speed corresponding to the minimum required thrust and minimum required throttle, in order to achieve a more energy-efficient steady climb.

Overall, the analysis of drone climb and balance states shows that although drones have the ability to climb slowly at low speeds and high pitch angles, their various balance states are very sensitive to changes in flight speed and climb angle. When the drone flies in this state, it is highly susceptible to external environmental interference, which requires high stability, maneuverability, and robustness of the controller.

(2) Analysis of the climbing envelope characteristics of unmanned aerial vehicles

Based on the above results of balancing the stable climb of the drone, we find the boundary points of the balancing state and draw the velocity climb angle envelope, velocity angle of attack envelope, and pitch angle throttle envelope of the drone climbing process, as shown in Figure 18.

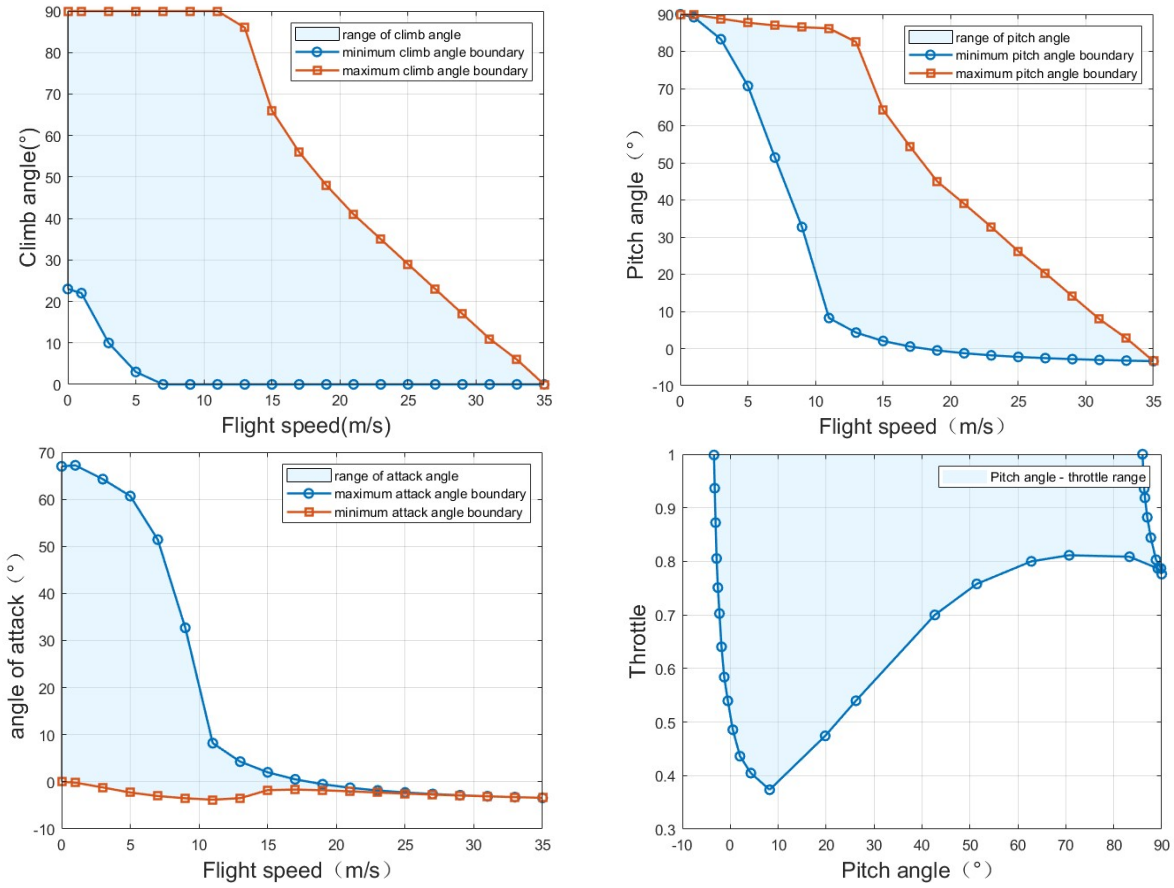


Figure 18. Stable climbing balance envelope.

According to the minimum climb angle boundary, when the drone's flight speed is less than 7 m/s, it does not have the ability to fly at a small angle. As the flight speed increases, the minimum climb angle boundary gradually decreases from around 20° to zero. According to the maximum climb angle boundary, when the flight speed of the drone is less than 11 m/s, the drone has the ability to climb vertically at a low speed. As the flight speed increases, its maximum climb angle boundary gradually decreases to 0. The trend of pitch angle changing with flight speed is basically consistent with the climb angle, but its reachable boundary range is smaller than the climb angle. According to the flight speed angle-of-attack flight envelope, when the drone climbs at a low speed and low climb angle,

a high-angle-of-attack state will occur. Therefore, it is recommended to require drones to perform flight missions within this angle of attack range, and the minimum climbing speed for drones is 7 m/s. According to the pitch angle throttle envelope obtained from the drone climb balancing, when the drone pitch angle is around 9°, the available throttle range that supports drone level flight or climb is the largest. As the pitch angle of the drone decreases, its minimum throttle boundary rapidly increases. As the pitch angle of the drone increases, its minimum throttle boundary gradually increases, and the maximum throttle boundary rapidly decreases from 1 when the pitch angle approaches 90°.

(3) Design of Takeoff and Climbing Control Strategy for Drones

Based on the analysis of the balancing results of the drone climbing state, the trend of each balancing state variable with speed, and the achievable boundary of the balancing state variable in the previous text, the climbing angle range of 30°~90° is selected to further analyze the drone power and climbing rate, in order to find the optimal drone climbing strategy. The motor power, climb rate, and total energy output of the motor during the stable climb process of the drone vary with the flight speed as shown in the Figure 19.

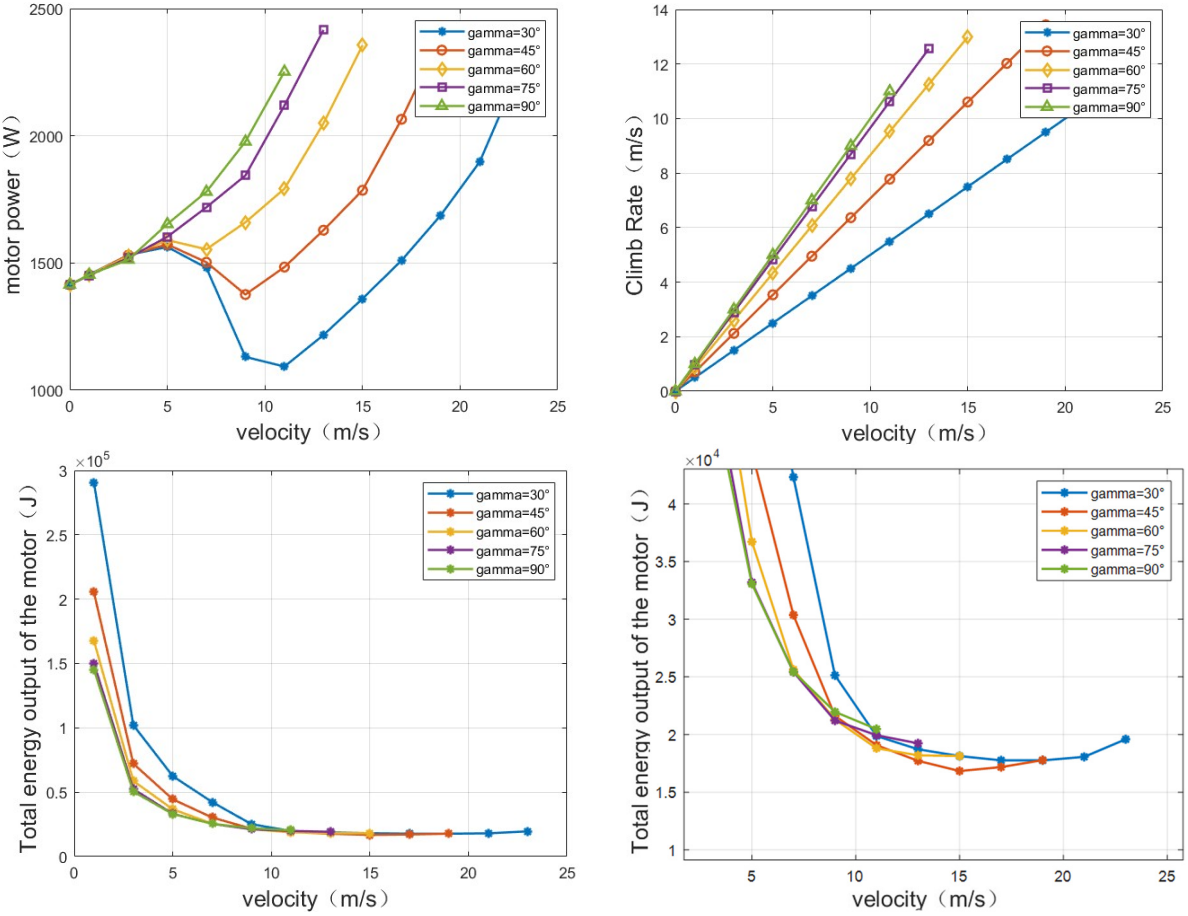


Figure 19. Power, climb rate, and energy variation curves with speed.

Analyzing the curve of motor power variation with speed, it can be seen that its trend is basically consistent with the throttle opening. When the climb angle approaches 90°, the motor power increases monotonically with the increase in drone flight speed. When the climb angle is slightly small, the motor power decreases first and then increases with the increase in the drone's flight speed. Each climb angle corresponds to a minimum required power and minimum power speed. Analyzing the curve of climb rate with speed variation, it can be seen that for the same climb angle, the climb rate increases correspondingly with

the increase in flight speed. At the same flight speed, the larger the climb angle, the higher the climb rate.

Based on the above analysis, this article will design three takeoff climb strategies for MY-UAV, namely, minimum-power climb, maximum-climb-rate climb, and minimum-energy climb.

To obtain the minimum-power climb strategy, search for the minimum power point in the upper-left figure, which corresponds to the unmanned aerial vehicle climb state point with a flight speed of 11 m/s and a climb angle of 30°. When the drone climbs steadily in this state, the required power is minimized. At this time, the drone climb rate is 5.5 m/s, and the motor output power is 1093 W.

To obtain the maximum-climb-rate climb strategy, search for the point of maximum climb rate in the upper-right figure, which corresponds to the unmanned aerial vehicle climb state point with a flight speed of 19 m/s and a climb angle of 45°. When the drone climbs steadily in this state, the maximum climb rate is obtained, with a climb rate of 13.435 m/s and a motor output power of 2389 W.

To obtain the minimum-energy climb strategy, it is necessary to calculate and analyze the total energy consumed by the drone during the entire takeoff climb phase. Due to the very short process of unmanned aerial vehicles from takeoff and landing to acceleration to steady-state climb speed, it is believed that the impact of the energy consumed during this process on the total energy consumed during the climb phase can be ignored. Therefore, only the total energy required for the climbing phase of the drone is evaluated. Given the vertical altitude required for climbing during the climbing phase is h, the climbing time is $t = h/v_d$ calculated based on the climbing rate. Combined with the motor power at each state point, the total energy output of the motor $E = P \cdot t$ in the climbing section is obtained. We then find the state point where the total energy output of the motor is minimized, which is the minimum-energy climb state point. The minimum point of total energy output of the motor is the unmanned aerial vehicle climb state point corresponding to a flight speed of 15 m/s and a climb angle of 45°. When the drone climbs steadily in this state, the climb rate is 10.6 m/s, the motor output power is 1786 W, and the total energy required for the motor output to climb 100 m is 16,838.6 J.

Finally, three unmanned aerial vehicle takeoff climb strategies were determined: minimum-power climb, maximum-climb-rate climb, and minimum-energy climb. A summary is shown in Table 2:

Table 2. Takeoff and climbing strategies for MY-UAV drones.

Takeoff Climb Strategy	Velocity /(m/s)	Climbing Angle/(°)	Climbing Rate/(m/s)	Power /(W)
Minimum-power climb	11	30	5.5	1093
Maximum-climb-rate climb	19	45	13.435	2385
Minimum-energy climb	15	45	10.6	1786

3.2. Analysis of Downward Performance and Design of Steep Descent Control Strategy

In order to meet the requirements of mission scenarios, the MY-UAV's landing method is different from the conventional drone's sliding landing but completes the landing task through a steep descent with a large pitch angle.

(1) Performance analysis of drone glide

Firstly, the force situation during the sliding process of the distributed-propeller fixed-wing unmanned aerial vehicle is analyzed. Figure 20 is a schematic diagram of the force situation during the sliding state of the unmanned aerial vehicle.

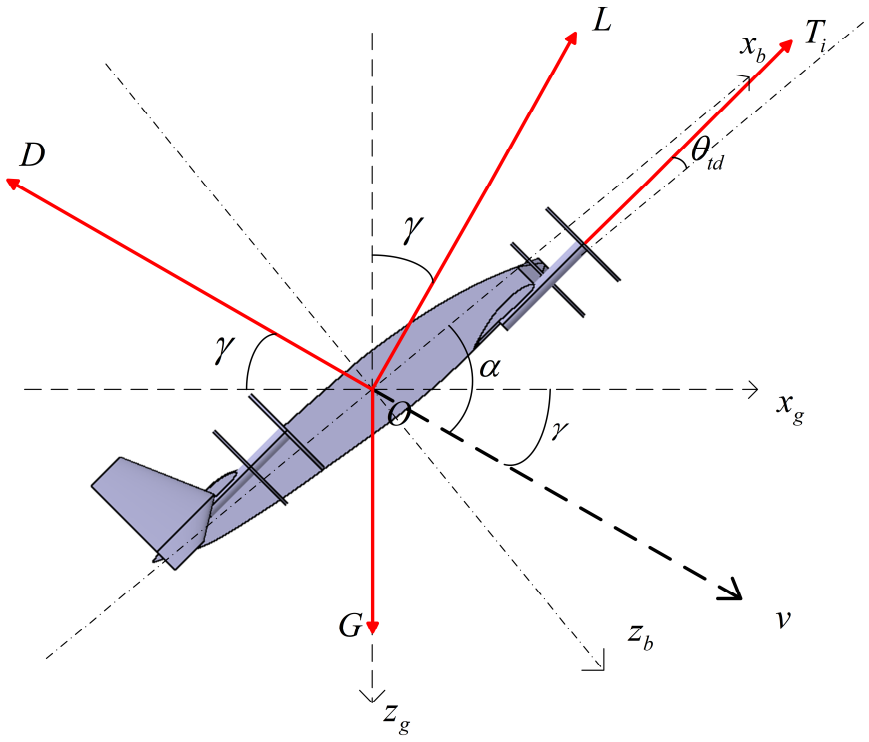


Figure 20. Schematic diagram of force on MY-UAV in sliding state.

The force situation is analyzed during the sliding process of a distributed-propeller fixed-wing unmanned aerial vehicle:

$$\begin{cases} L\sin\gamma - D\cos\gamma \\ \quad + \sum_{i=1}^{8} T_{xi}\cos(\alpha-\gamma) + \sum_{i=1}^{8} T_{zi}\sin(\alpha-\gamma) = 0 \\ m + \sum_{i=1}^{8} m_{Ti} = 0 \\ -L\cos\gamma - D\sin\gamma \\ \quad - \sum_{i=1}^{8} T_{xi}\sin(\alpha-\gamma) + \sum_{i=1}^{8} T_{zi}\cos(\alpha-\gamma) + G = 0 \end{cases} \tag{17}$$

The relationship between the balanced state variables and flight speed and climb angle is shown in Figure 21:

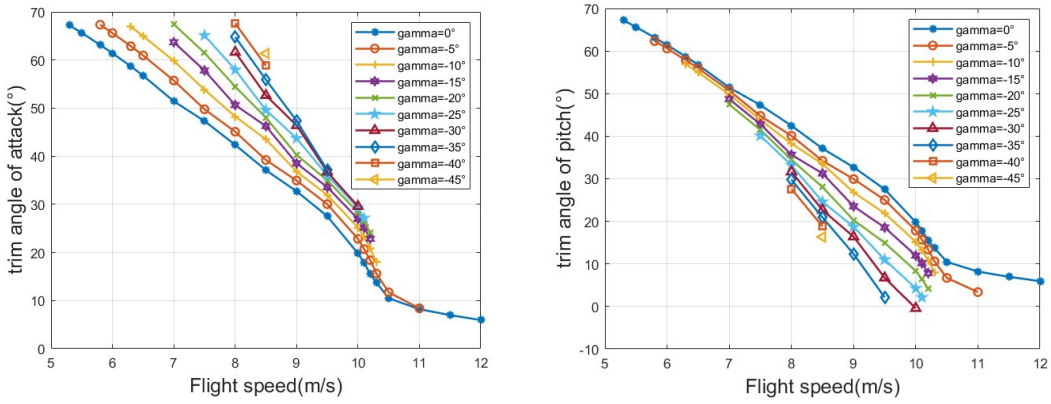


Figure 21. *Cont.*

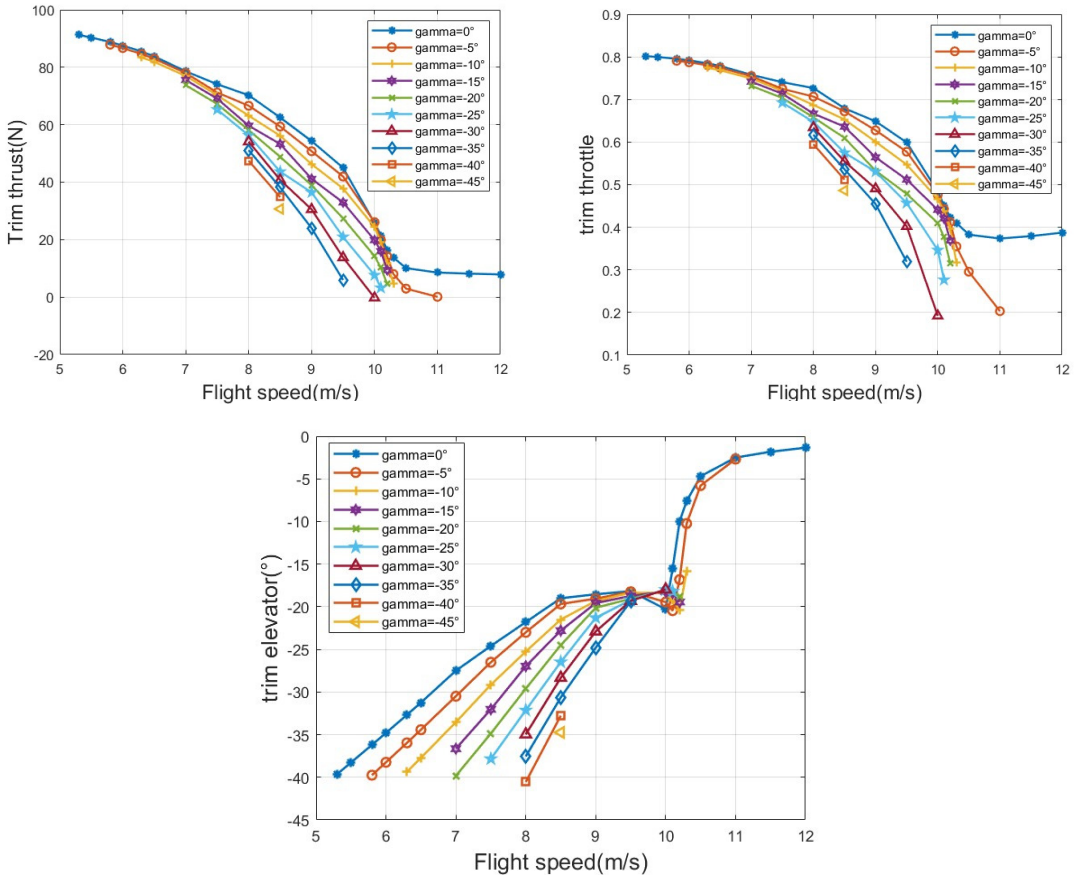


Figure 21. Curve of the variation in the glide balance state variable with flight speed.

At the same glide angle, as the drone's flight speed increases, its glide balance angle of attack decreases accordingly; at the same flight speed, as the glide angle of the drone increases, its glide balance angle of attack also increases accordingly.

At the same glide angle, as the drone's flight speed increases, the balanced glide pitch angle decreases accordingly; at the same flight speed, as the glide angle of the drone increases, its trim pitch angle also decreases accordingly.

Therefore, to ensure that the drone can glide with a large glide angle and have sufficient glide balance margin, it is recommended that the flight speed of the drone during glide should be maintained within the range of 6.3 m/s to 10.3 m/s. This allows for a very narrow range of flight speeds, making it very difficult to control the steep descent process of drones.

The trend of drone balancing thrust changing with flight speed and glide angle is basically consistent with the trend of balancing throttle changing with flight speed and glide angle. It can be seen that within a certain range, the larger the glide angle and flight speed of the drone, the smaller the required thrust for balancing. Therefore, within the allowable range of glide speeds, from an energy perspective, it is recommended to complete the glide mission with a higher flight speed and glide angle.

Fixed glide angle, when the drone's flight speed approaches the minimum flight speed that can be balanced under the current glide angle, the absolute value of the glide balance elevator angle will be greater than 35° and close to the upper limit of the control surface angle. At this time, the drone's operating margin is very small, which is not conducive to the stable glide of the drone. At the same time, when the glide angle is greater than about 40°, within all speed ranges that can be balanced, the absolute value of the glide balance elevator deflection angle is greater than 32°, approaching the upper limit of the rudder deflection angle. Therefore, it is recommended that the glide angle of the drone should be kept within a range of 40° as much as possible.

(2) Analysis of the characteristics of drone glide envelopes

Find the boundary points for the stable glide of the drone, and draw the velocity glide angle envelope, velocity pitch angle envelope, and pitch angle throttle envelope of the drone glide process below a flight speed of 15 m/s, as shown in Figure 22.

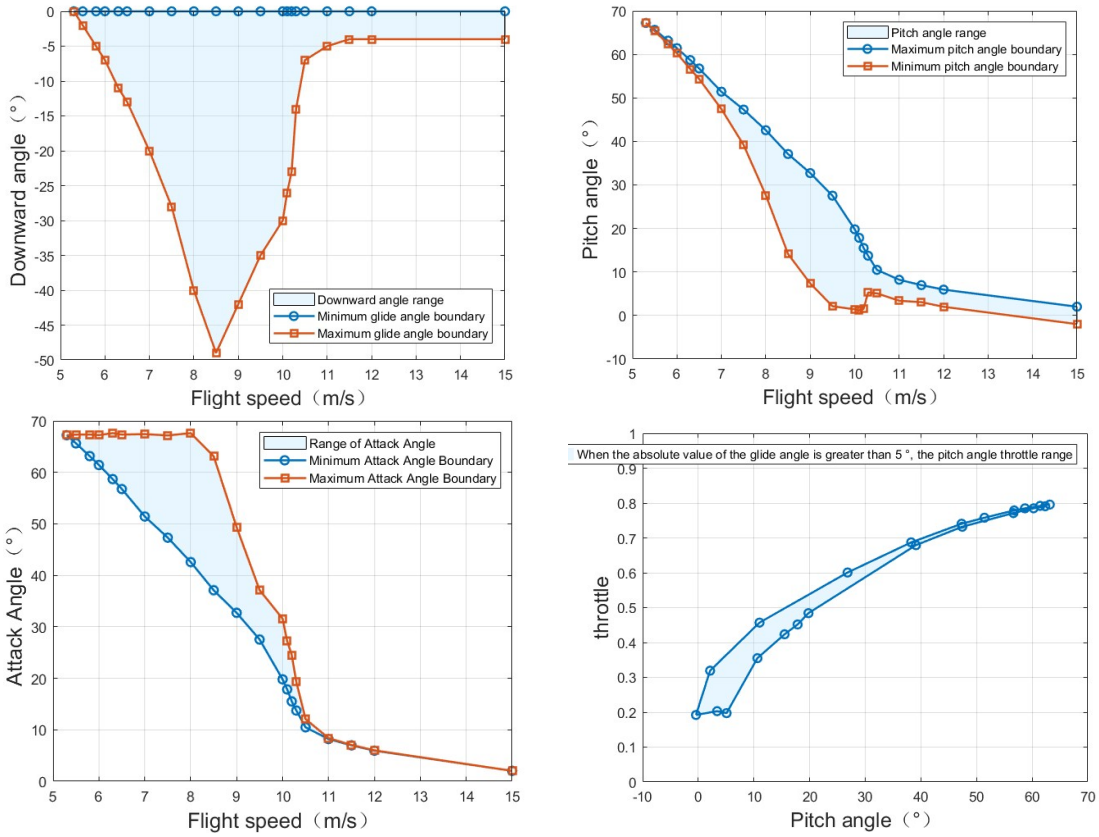


Figure 22. Stable sliding balance envelope.

As the flight speed increases, both the glide angle range and pitch angle range of the drone first increase and then decrease. If the drone is required to meet the task of steep descent with a large pitch angle, its glide angle should not be less than 10°, and the drone's glide flight speed should be considered within the range of 6.3 m/s to 10.3 m/s.

As the pitch angle of the drone increases, the available range of its throttle first increases and then decreases; when the pitch angle exceeds 40°, the available range of the throttle sharply decreases. The larger pitch angle corresponds to a smaller flight speed with the corresponding glide state. Based on the pitch angle velocity envelope mentioned earlier, it is recommended that the descent speed of the drone should not be less than 7.5 m/s.

In summary, based on the comparative analysis of the velocity glide angle envelope, velocity pitch angle envelope, and pitch angle throttle envelope during the descent process of unmanned aerial vehicles, it is recommended that the range of descent velocity for unmanned aerial vehicles be between 7.5 m/s and 10.3 m/s.

(3) Design of Control Strategy for Unmanned Aerial Vehicle Downward Landing

In order to meet the mission scenario requirements of drones, it is necessary to design landing trajectories with low energy consumption and short forward flight distance. The drone mission package includes takeoff, climb, cruise, descent, and steep descent. Assuming that the drone completes the takeoff climb task, it performs cruise flight at an altitude of 500 m and a speed of 15 m/s. When receiving the landing command, the drone needs to slow down from the current altitude until the landing task is completed. Below is an analysis of the descent rate, power, and process energy consumption of unmanned aerial

vehicles at different climb angles and speeds, in order to seek the optimal landing trajectory, as shown in Figure 23.

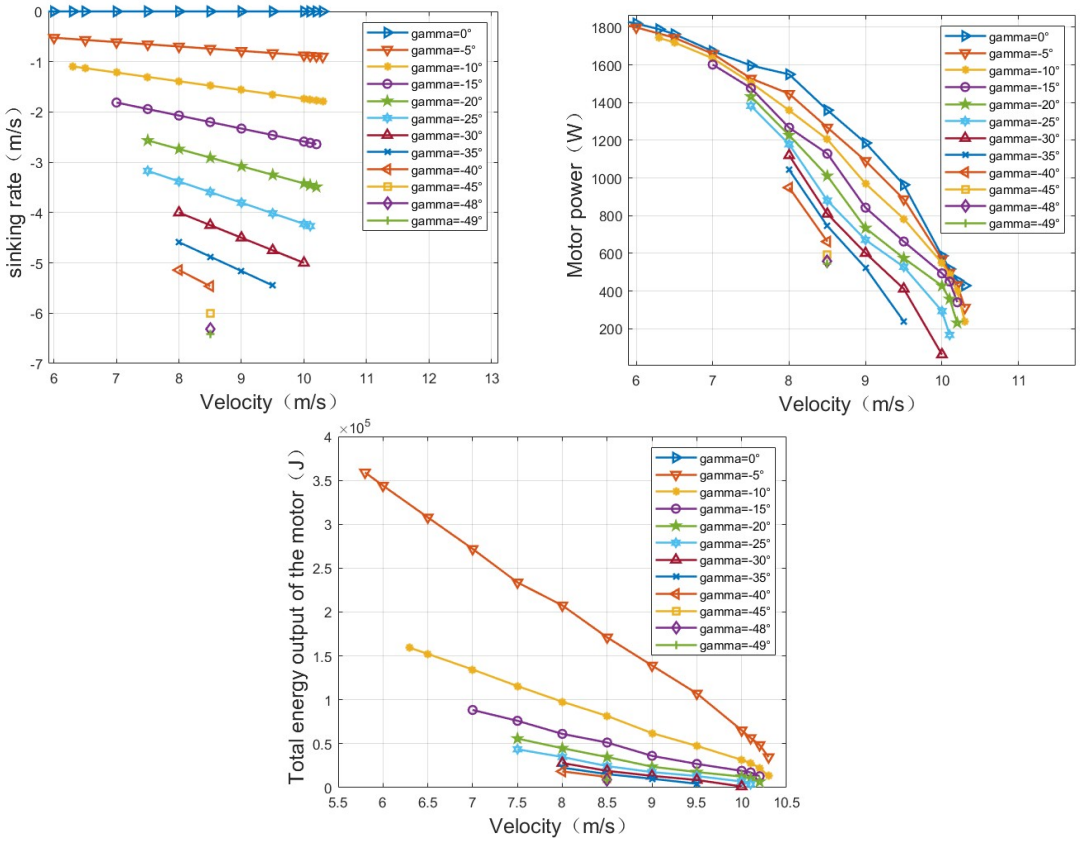


Figure 23. Curves of power, sinking rate, and energy variation with speed.

From the analysis of the above figures, it can be seen that the maximum sinking rate of the drone can reach around 6.5 m/s. As the sliding angle and flight speed decrease, the sinking rate of the drone decreases accordingly. Based on the performance and mission scenario requirements of the unmanned aerial vehicle in this article, the designed sinking rate during approach landing should not exceed 3 m/s. The output power of the drone motor and the total energy output of the descent stage motor both decrease correspondingly with increasing speed and descent angle.

Based on the above simulation results, this paper proposes an optimal steep descent strategy, which divides the UAV steep descent process into two stages:

① Low-power rapid decline stage. The main task of drones in this stage is to achieve the shortest distance altitude reduction with minimal energy consumption, that is, to seek the maximum sinking rate and minimum energy consumption decline state of drones within the allowable speed range. Assuming the starting altitude of the drone is 500 m and the landing target altitude in this stage is 50 m, the drone is designed to steadily glide at a $-40°$ glide angle, a flight speed of 8.5 m/s, and a sinking rate of 5.46 m/s. The state point has a balanced pitch angle of 18.8°, a balanced angle of attack of 58.8°, a balanced elevator deflection angle of $-32.8°$, and a balanced power of 662.6 W.

② High-power and low-sinking-rate landing phase. The main task of the drone in this stage is to achieve a minimum ground speed landing, which requires the drone to gradually reduce its flight speed with decreasing altitude and land at a sinking rate of nearly 0 m/s. The steep descent trajectory and changes in various state variables over time during the high-power, low-sinking-rate landing phase are shown in Figure 24.

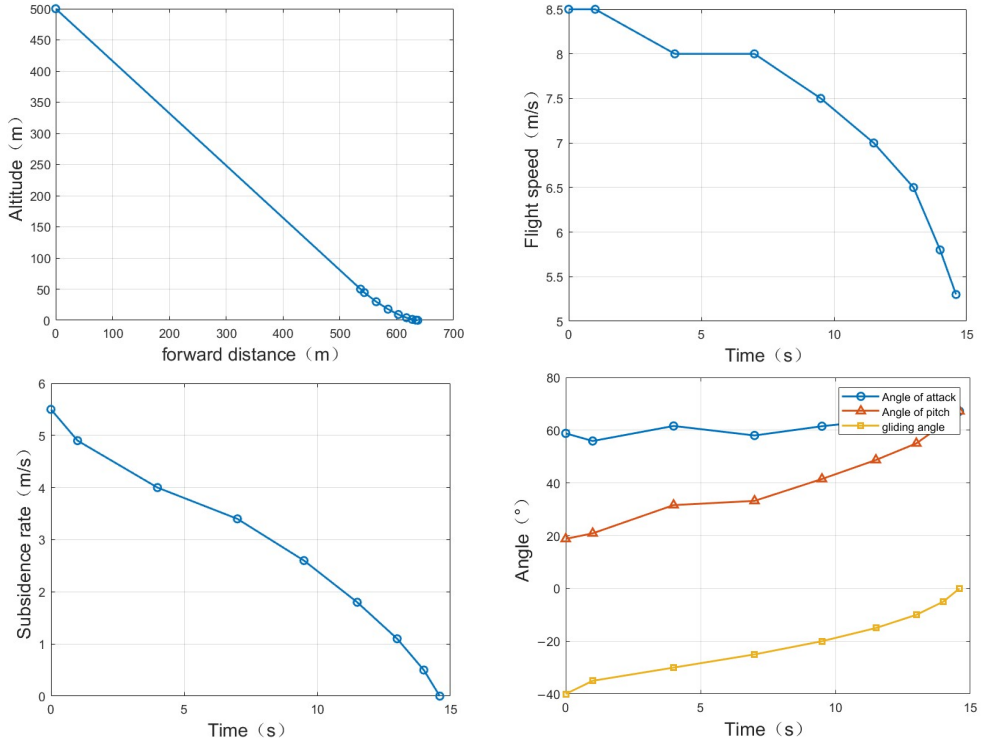


Figure 24. Changes in various state variables over time during the landing phase with high power and a low sinking rate.

4. Design and Simulation Flight of Control Law for Jumping and Steep Descent of Drones

4.1. Analysis of UAV Control Efficiency and Design of Control Scheme

Study the longitudinal and lateral turning torques generated by the differential power and rudder deflection of unmanned aerial vehicles, and select the optimal control strategy based on the operational efficiency of each control component.

For longitudinal pitch motion, lateral roll motion, and yaw motion of the drone, calculate the incremental rotational torque caused by the deflection of the elevator, aileron, and rudder surfaces and the power differential, and plot their curves as a function of the angle of attack, as shown in Figures 25–27:

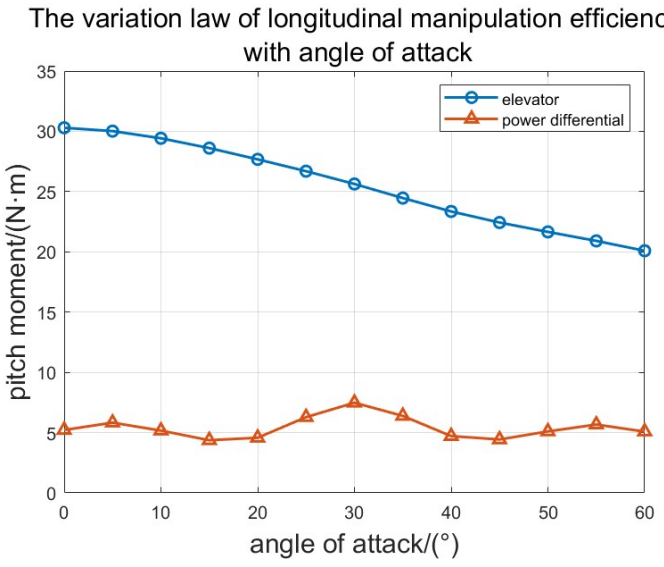


Figure 25. Variation law of pitch control efficiency with angle of attack.

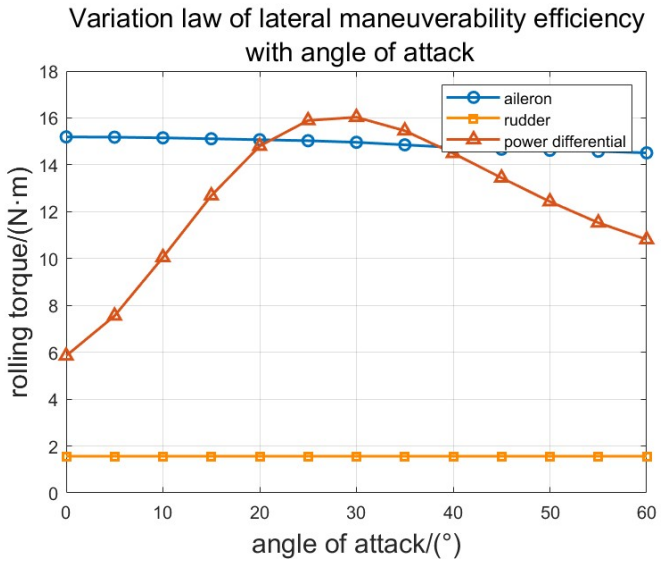


Figure 26. Variation law of roll control efficiency with angle of attack.

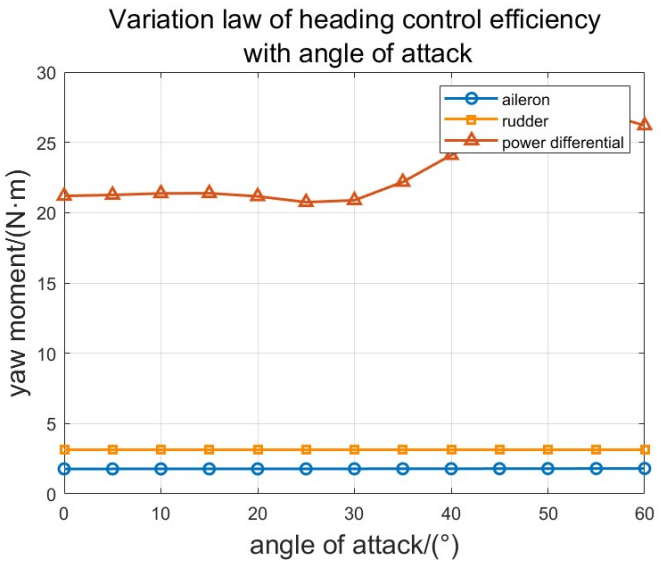


Figure 27. Variation law of yaw control efficiency with angle of attack.

According to the simulation results of the longitudinal control efficiency of the drone, it can be concluded that the power differential control efficiency of the drone during longitudinal pitch motion is much lower than the control efficiency of elevator deflection. For lateral control, the control efficiency generated by aileron deflection is already significant enough, and in most flight states, it is much higher than power differential and rudder deflection. For heading control, the yaw moment increment caused by dynamic differential is greater than rudder deflection within the range of cruise speed of UAV below 15 m/s.

Thus, the drone takeoff and landing control scheme was determined, which only uses elevator pitch control for longitudinal control of the drone, without considering differential control of the front and rear propellers. The lateral control of the drone only uses aileron roll control, without considering the differential control of the left and right propellers. The heading control of the drone adopts a combination of rudder yaw control and left- and right-propeller power differential control.

4.2. Design of UAV Takeoff and Landing Control Law

The longitudinal attitude control of the drone mainly consists of a pitch angle control loop, including pitch rate feedback and pitch angle feedback. The controller block diagram is shown in Figure 28:

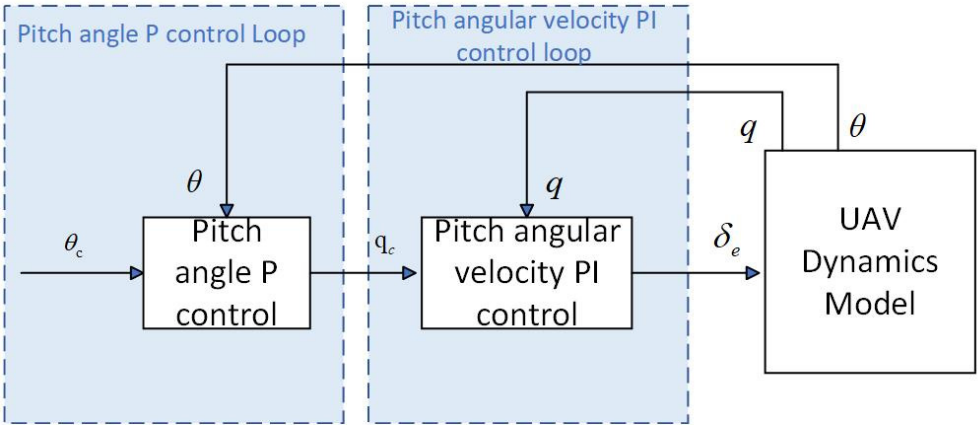


Figure 28. Schematic diagram of longitudinal attitude control loop based on PID.

The pitch angle control adopts a cascade PID control method, with the inner loop being pitch angle velocity PI control and the outer loop being pitch angle P control. The control law is as follows:

$$\begin{cases} q_c = k_\theta(\theta_c - \theta) \\ \delta_e = (k_q + k_{qi} \cdot \frac{1}{s})(q - q_c) \end{cases} \quad (18)$$

where k_θ is the proportional coefficient of the pitch angle controller, k_q and k_{qi} are the proportional coefficient and integral coefficient of the pitch angular velocity controller, respectively; $k_\theta = 1.5$, $k_{qi} = 0.01$, $k_q = 1.5$.

The outer-loop longitudinal position controller includes height control and speed control. The height control input is the desired height and current height, and the output is the desired pitch angle. The speed control input is the desired speed and current drone airspeed, and the output is the desired throttle opening. The longitudinal position control block diagram based on PID is shown in Figure 29:

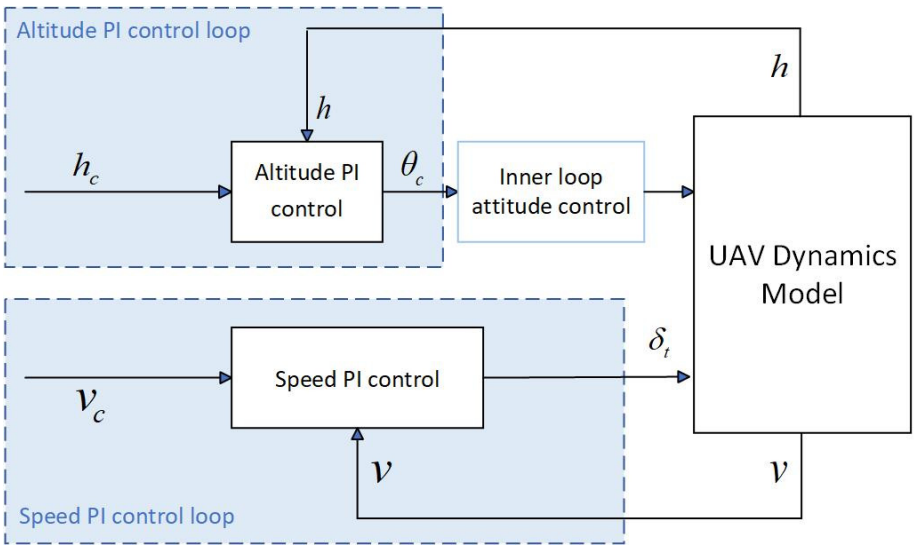


Figure 29. Schematic diagram of longitudinal position control circuit based on PID.

The drone altitude control adopts PI control, and the control law is as follows:

$$\theta_c = (k_h + k_{hi} \cdot \frac{1}{s})(h - h_c) \tag{19}$$

$$k_h = 1.5,\ k_{hi} = 0.02$$

The speed control of the drone adopts PI control, and the control law is as follows:

$$\delta_t = (k_v + k_{vi} \cdot \frac{1}{s})(v_c - v) \cdot k_{\delta_t} \tag{20}$$

$$k_v = 0.5,\ k_{vi} = 1.5,\ k_{\delta_t} = 0.01$$

The lateral heading control of unmanned aerial vehicles includes roll control and yaw control. Roll control tracks the roll angle command signal through roll angle feedback and roll angle velocity feedback. The control logic is the same as the pitch angle control, using cascade PID control, with the inner loop being PI control of roll angle velocity and the outer loop being P control of roll angle. Yaw control improves heading stability through sideslip angle feedback At the same time, the deviation signal generated by the yaw rate signal and the yaw rate coordination signal during rolling is used to realize coordinated turning, and the damping characteristics are improved. The joint control of rudder and dynamic differential is adopted. The controller block diagram is shown in Figure 30:

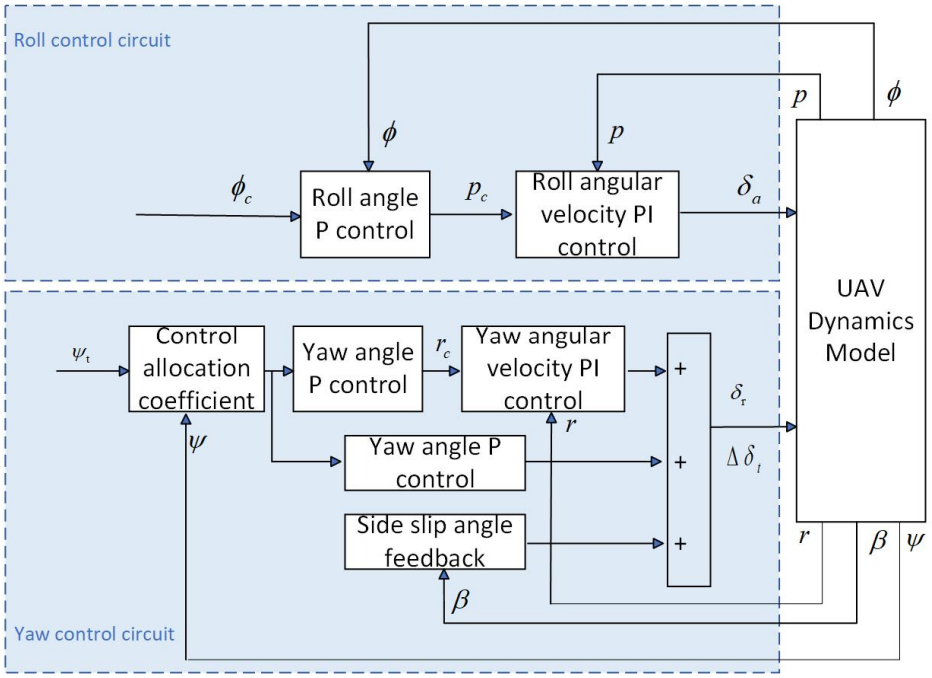


Figure 30. Block diagram of lateral heading attitude control circuit.

The control law design for the lateral heading roll control circuit is as follows:

$$\begin{cases} p_c = k_\phi(\phi_c - \phi) \\ \delta_a = (k_p + k_{pi} \cdot \frac{1}{s})(p - p_c) \end{cases} \tag{21}$$

where $k_\phi = 2.5$, $k_{pi} = 0.01$, and $k_p = 0.5$.

The lateral yaw control circuit is divided into rudder control and dynamic differential control. The input of the overall loop is the expected yaw angle ψ_c output by the outer-loop lateral heading position control, as well as the expected roll angular velocity of the unmanned aerial vehicle. The expected roll angular velocity is set as 0, and the

difference between the current yaw angle ψ and the expected yaw angle ψ_c is the yaw angle error, $\psi - \psi_c$, with the following values:

$$\psi - \psi_c = \begin{cases} (\psi - \psi_c) + 360, & \psi - \psi_c < -180 \\ \psi - \psi_c, & -180 \le \psi - \psi_c \le 180 \\ (\psi - \psi_c) - 360, & \psi - \psi_c > 180 \end{cases} \tag{22}$$

Based on the results $\psi - \psi_c$, it is necessary to allocate weights between rudder control and dynamic differential control, designed $k_{\psi_\delta_r}$ as the weight coefficients for rudder control yaw and $k_{\psi_\delta_t} = 1 - k_{\psi_\delta_r}$ as the dynamic differential control yaw. The weight coefficients are multiplied by the yaw angle error to obtain the yaw angle error of the rudder circuit and the yaw angle error of the power differential circuit, respectively:

$$\Delta\psi_{\delta_r} = k_{\psi_\delta_r} \cdot (\psi - \psi_c) \tag{23}$$

$$\Delta\psi_{\delta_t} = k_{\psi_\delta_t} \cdot (\psi - \psi_c) \tag{24}$$

where it is taken that $k_{\psi_\delta_r} = 0.4$ and $k_{\psi_\delta_t} = 0.6$.

In addition to the yaw angle error, the rudder control circuit also introduces the current yaw rate and the expected yaw rate as inputs to obtain the yaw rate error and outputs the rudder deflection command. The control law is as follows:

$$\begin{cases} r_{c_\delta_r} = k_{\Delta\psi_\delta_r} \cdot \Delta\psi_{\delta_r} \\ \delta_r = (k_{r_\delta_r} + k_{ri_\delta_r} \cdot \frac{1}{s})(r - r_{c_\delta_r}) + k_{\beta_\delta_r} \cdot \beta \end{cases} \tag{25}$$

where $k_{\Delta\psi_\delta_r}$ is the proportional coefficient of yaw angle error rudder, $k_{r_\delta_r}$ and $k_{ri_\delta_r}$ are the proportional coefficient and integral coefficient of yaw angular velocity error, and $k_{\beta_\delta_r}$ is the feedback coefficient of the sideslip angle; $k_{\Delta\psi_\delta_r} = 2.5$, $k_{r_\delta_r} = 0.5$, $k_{ri_\delta_r} = 0.01$, $k_{\beta_\delta_r} = 2$.

The input of the power differential control circuit only uses the yaw angle error control quantity, and the output is $\Delta\delta_t$, the power difference between the left and right propellers of the drone. When the power differential quantity of the drone is defined as positive, the throttle opening of the left propeller is $\delta_t + \Delta\delta_t$, and the throttle opening of the left propeller is $\delta_t - \Delta\delta_t$; that is, a positive power difference will cause the drone to generate a negative yaw moment. The power differential only uses a proportional controller to eliminate yaw angle errors, and the control law is as follows:

$$\Delta\delta_t = k_{\delta_t} \cdot k_{\Delta\psi_\delta_t} \cdot \Delta\psi_{\delta_t} \tag{26}$$

where k_{δ_t} is the conversion coefficient from the angle to the throttle amount and $k_{\Delta\psi_\delta_t}$ is the power differential proportional coefficient of yaw angle error; $k_{\delta_t} = 0.01$, $k_{\Delta\psi_\delta_t} = 0.5$.

Due to the need for precise yaw control, this article uses a traditional PI controller for the lateral heading trajectory control of the outer loop of the drone. The input is the desired position x_{ec} and the current drone position x_e, and the output is the desired yaw angle ψ_c of the drone. A block diagram of the controller is shown in Figure 31:

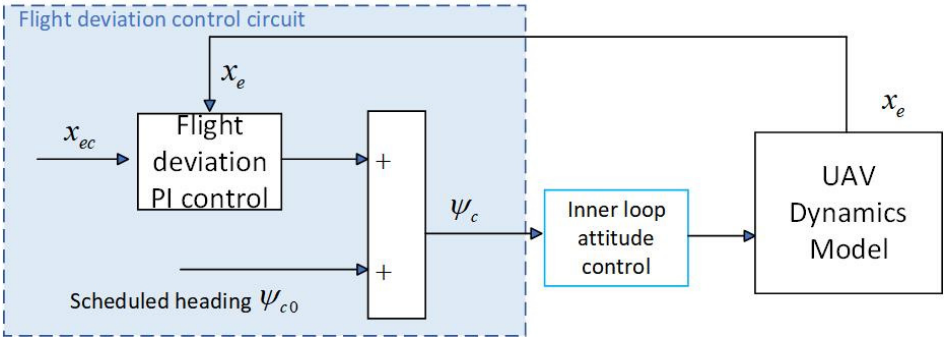


Figure 31. Block diagram of lateral heading position control circuit.

The control law for the lateral heading trajectory of the drone's outer loop is as follows:

$$\psi_c = (k_{x_e\psi} \cdot k_{x_e} + k_{x_ei} \cdot \frac{1}{s})(x_e - x_{ec}) + \psi_{c0} \quad (27)$$

where ψ_{c0} is the initial predetermined heading angle of the drone, $k_{x_e\psi}$ is the conversion coefficient from the distance to the angle, and k_{x_e} and k_{x_ei} are the proportional coefficient and integral coefficient of the PI controller, respectively; $k_{x_e} = -5$, $k_{x_ei} = -0.05$.

4.3. Digital Simulation Flight During Drone Takeoff and Landing Phase

Due to the task requirement of achieving fast climb with less energy during the takeoff and climb process of the drone, precise altitude tracking is not required. Therefore, only the attitude controller designed in Section 3.2 is currently considered to control the takeoff process of the drone. Firstly, a digital simulation is conducted on the takeoff strategy with minimum-energy climb (flight speed of 15 m/s, climb angle of 45°, and climb rate of 10.6 m/s) under ideal conditions. The simulation results are shown in Figure 32:

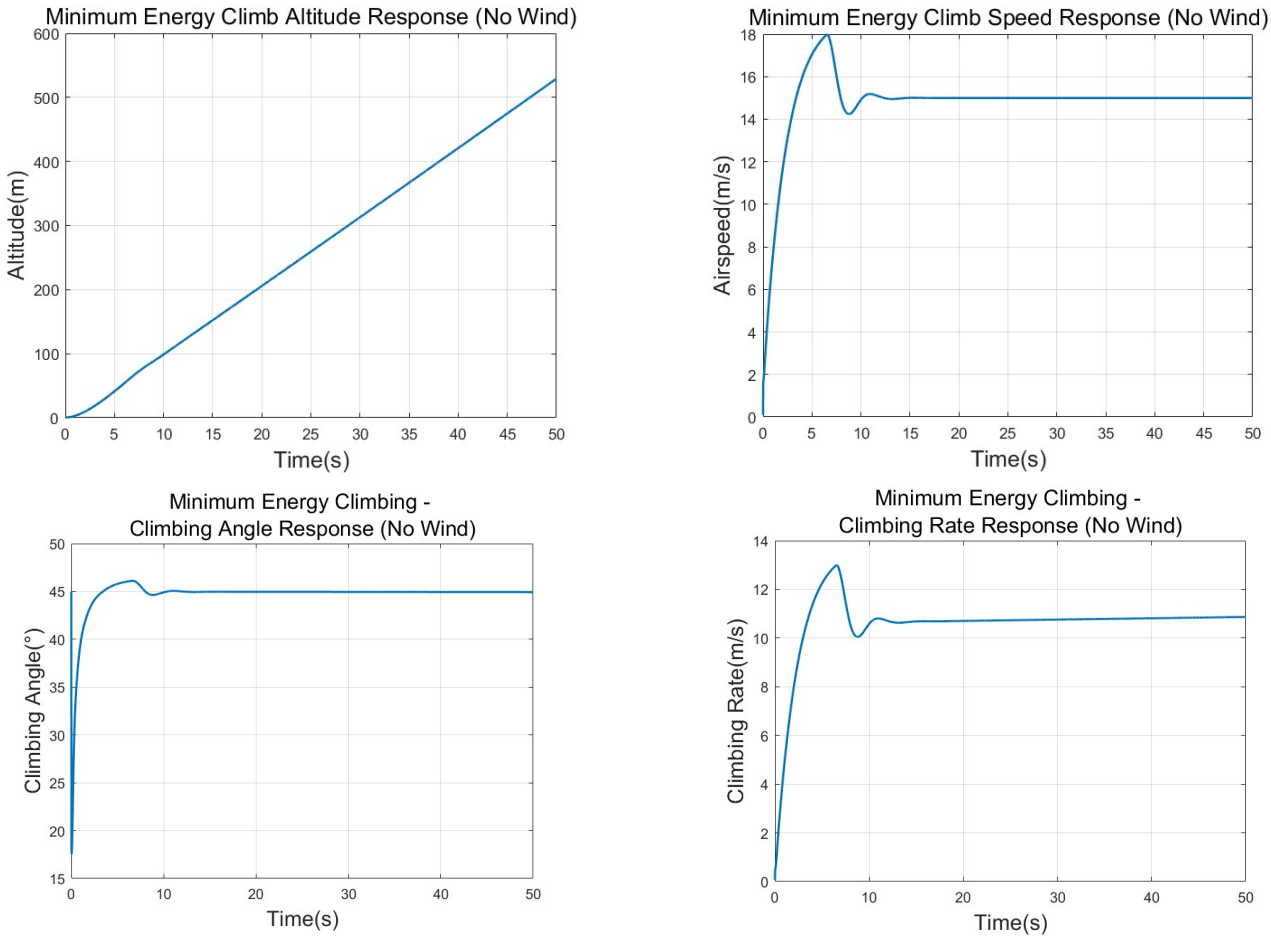


Figure 32. *Cont.*

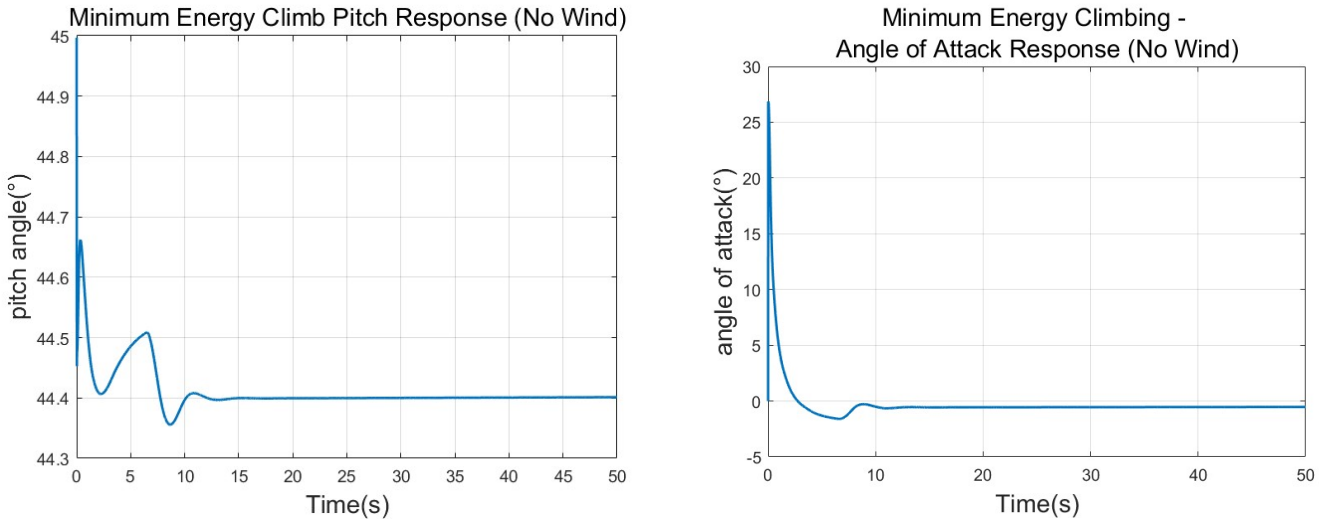


Figure 32. Digital simulation of takeoff climb process.

According to the simulation results of the takeoff process, it can be seen that the drone can basically complete the takeoff climb task according to the designed takeoff climb strategy.

During the takeoff phase, the drone takes about 13 s to jump from the ground to a stable climbing state and climbs a total height of about 120 m. At the moment of takeoff and landing, the maximum angle of attack of the drone reaches about 28°, but it quickly decreases to the stall angle of attack range within 1 s. Therefore, it can be considered that there is no high-angle-of-attack state of the drone during takeoff and climb. It takes about 48 s for the drone to climb to a cruising altitude of 500 m, and during the stable climb phase, the drone's climb state is maintained at a 45° climb angle, 15 m/s airspeed, −0.56° angle of attack, and 10.7 m/s climb rate, meeting the design requirements for the drone's takeoff mode. The controller has good performance.

A complete simulation model of the glide slope controller is established, and a digital simulation of the entire process of drone descent is conducted. The response of each state variable is shown in Figure 33:

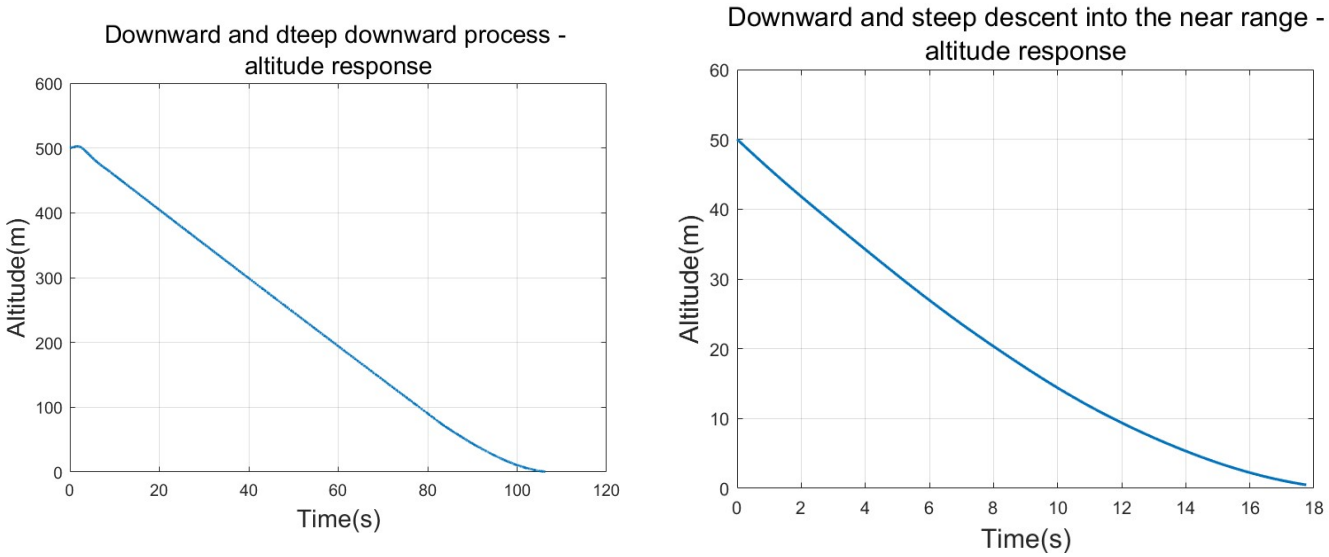
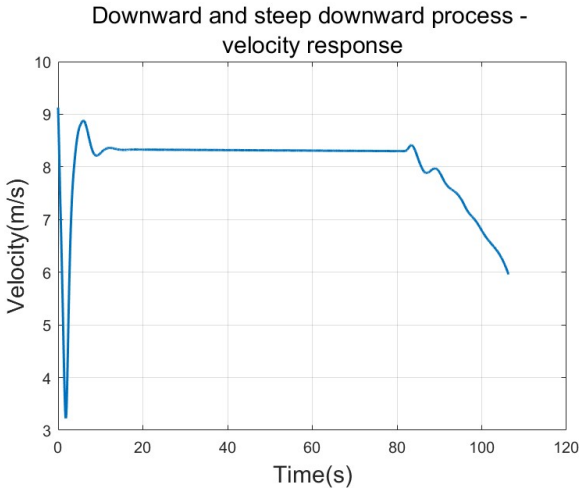
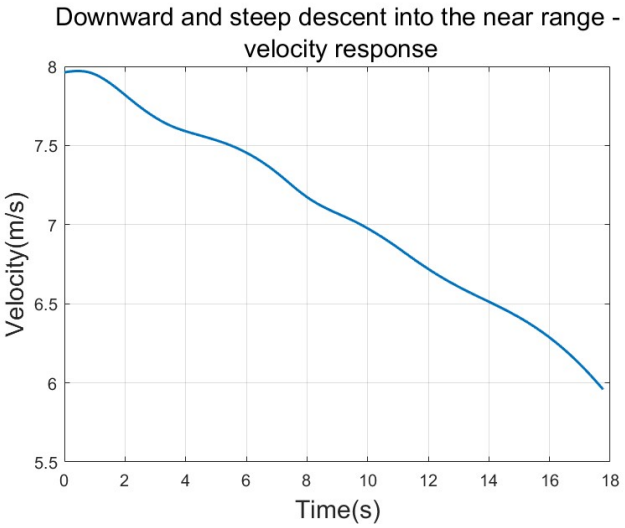
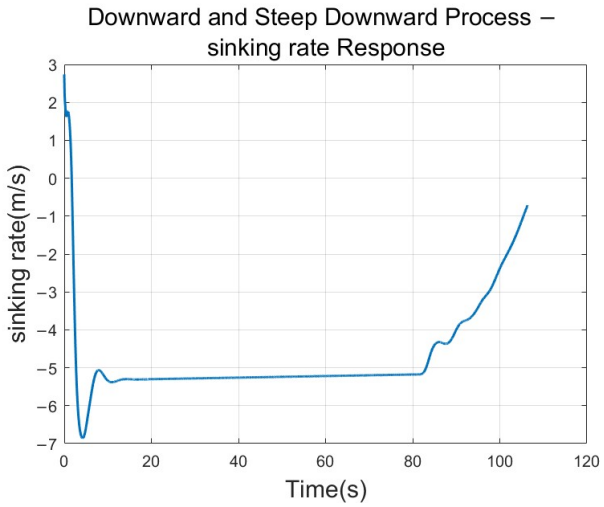
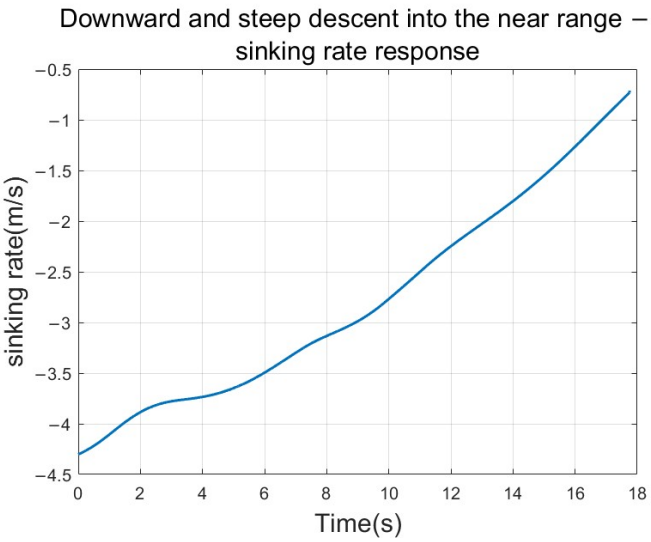


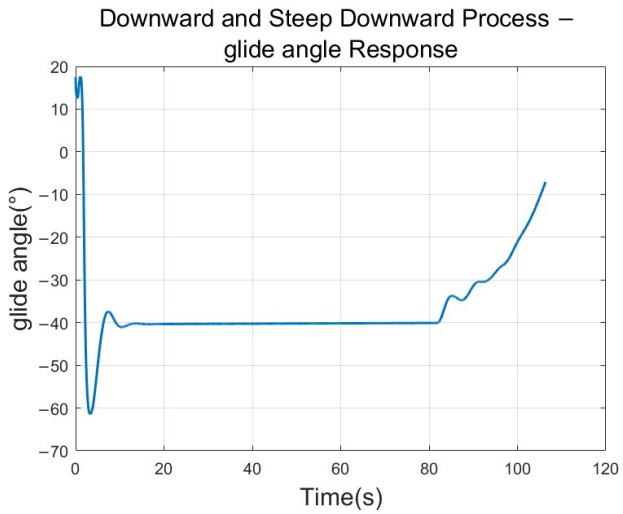
Figure 33. *Cont.*











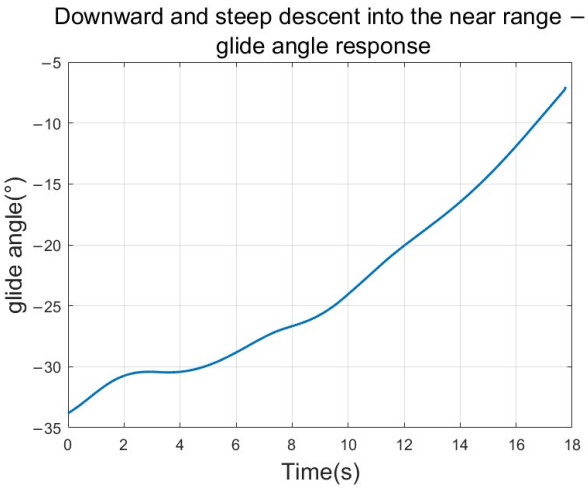


Figure 33. *Cont.*

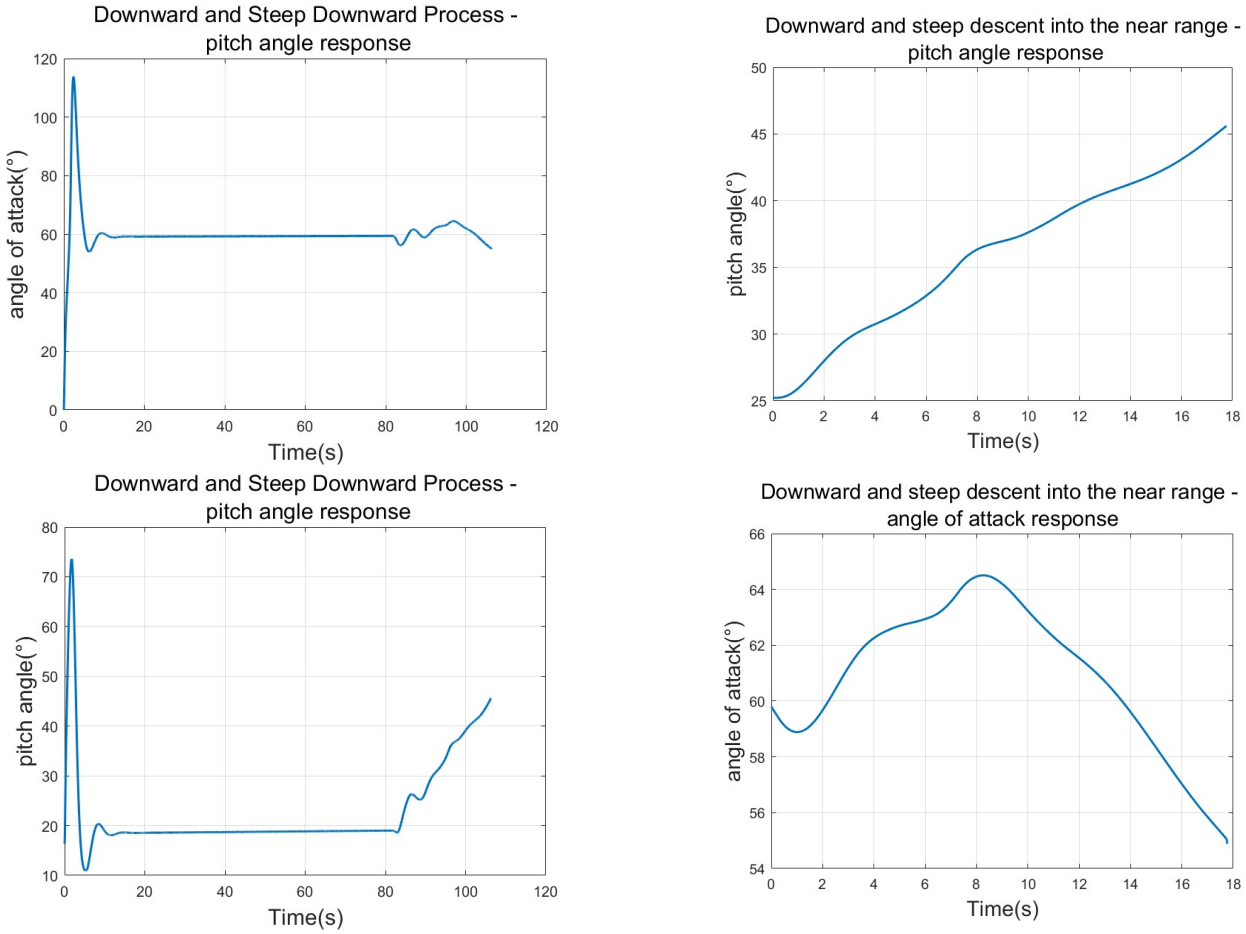


Figure 33. Digital simulation of the steep descent process.

The simulation results show that, during the approach process, the drone is in a low-speed high-angle-of-attack state, and the aerodynamic force of the drone is weakened. Longitudinal force balance is achieved by raising the head and increasing the throttle, and the pitch angle slowly increases from around 19° to around 45°; the sliding angle slowly decreases from around 40° to around 7°; and the fluctuation range of the angle of attack is around 5°. The descent into the near range takes about 18 s, with a drone speed of about 5.8 m/s when touching the ground, a sinking rate of about 0.8 m/s, and a descent angle of about 7°. It can safely complete the descent flight mission according to the designed descent strategy.

5. Conclusions

Aiming at the special steep ascent and descent flight process of distributed dynamic fixed wing UAV, this paper carried out the UAV dynamics modeling, jump and descent performance analysis, control strategy design, control law design and flight simulation research. The main research conclusions are as follows:

(1) Considering the influence of propeller slipstreams on the local angle of attack, sideslip angle, and velocity distribution, a coupled distributed dynamic slipstream model of the entire aircraft aerodynamic force and torque was established, and the lift model in the slipstream area was modified through ground slipstream experiments. Further ground sliding tests and low-speed climbing flight tests were conducted using experimental prototypes, and the experimental data showed that the established unmanned aerial vehicle (UAV) maneuvering mechanics model can accurately reflect the motion laws of the UAV.

(2) Through simulation analysis of the stability and dynamic control characteristics of the drone's static control, as well as the balancing characteristics during takeoff and

descent, it is confirmed that the drone has the ability to climb at low speeds with small climb angles and large pitch angles, as well as the ability to descend sharply at large angles.

(3) Based on the control capability of distributed-power fixed-wing unmanned aerial vehicles equipped with multiple power sources and control surfaces, a comparative analysis was conducted on the longitudinal and lateral heading control efficiency of the UAV's rudder deflection and power differential, as well as the impact of the UAV's angle of attack on the control efficiency of each rudder surface and power differential. A control scheme was determined to use "elevator for longitudinal control, ailerons for lateral control, and a combination of left and right power differential and rudder for heading control".

(4) Attitude and trajectory control laws for distributed-power takeoff and descent unmanned aerial vehicles were designed, and digital simulation research on the takeoff and landing stages of unmanned aerial vehicles was completed. The digital flight simulation results show that both the attitude controller and position controller of the drone have fast response capability and strong robustness. Based on the designed takeoff and landing controller, the drone can basically track the drone's jump and steep descent strategy and complete the jump and steep descent task.

Author Contributions: Conceptualization, Y.G. and X.X.; methodology, X.C. and Y.G.; software, X.C. and Y.H.; formal analysis, X.C.; writing—original draft preparation, Y.G., X.C. and X.X.; writing—review, X.X. and Y.H.; Visualization, X.C. and Y.H.; supervision, Y.G., X.C. and X.X.; project administration, X.X. All authors have read and agreed to the published version of the manuscript.

Funding: The research was funded by the Shaanxi Natural Science Research Program (No. 2023-YBGY-373) and the National Key Laboratory of Autonomous Intelligent Unmanned Systems (No. 2024-SRIAS-KF-010).

Institutional Review Board Statement: Not applicable.

Informed Consent Statement: Not applicable.

Data Availability Statement: The data presented in this study are available in the figures shown in the present article.

Conflicts of Interest: Author Yansheng Geng was employed by the company Aviation Industry Corporation of China Ltd. and author Xinxin Chen was employed by the company Xi'an ASN Technology Group Co., Ltd. The remaining authors declare that the research was conducted in the absence of any commercial or financial relationships that could be construed as a potential conflict of interest.

References

1. Kim, H.D.; Perry, A.T.; Ansell, P.J. A Review of Distributed Electric Propulsion Concepts for Air Vehicle Technology. In Proceedings of the 2018 AIAA/IEEE Electric Aircraft Technologies Symposium, Cincinnati, OH, USA, 12–14 July 2018. [CrossRef]
2. Zhang, Y.; Zhou, Z.; Wang, K.; Fan, Z. Influence of distributed power system parameters on the aerodynamic characteristics of a blended-wing-body UAV. *J. Northwestern Polytech. Univ.* **2021**, *39*, 17–26. [CrossRef]
3. Wagter, C.D.; Remes, B.; Smeur, E.; van Tienen, F.; Ruijsink, R.; van Hecke, K.; van der Horst, E. The NederDrone: A hybrid lift, hybrid energy hydrogen UAV. *Int. J. Hydrogen Energy* **2021**, *46*, 16003–16018. [CrossRef]
4. North, D.D.; Busan, R.C.; Howland, G. Design and Fabrication of the Langley Aerodrome No. 8—Distributed Electric Propulsion VTOL Testbed. In Proceedings of the AIAA SciTech Conference, Orlando, FL, USA, 6–10 January 2020.
5. Courtin, C.; Mahseredjian, A.; Dewald, A.J.; Hansman, J.R. A Performance Comparison of eSTOL and eVTOL Aircraft. In Proceedings of the AIAA AVIATION 2021 FORUM, Online, 2–6 August 2021. [CrossRef]
6. Nederlof, R. Improved Modeling of Propeller-Wing Interactions with a Lifting-Line Approach. Master's Thesis, Delft University of Technology, Delft, The Netherlands, 2020.
7. Khan, W.; Nahon, M. Development and Validation of a Propeller Slipstream Model for Unmanned Aerial Vehicles. *J. Aircr.* **2015**, *52*, 1985–1994. [CrossRef]
8. Chiappinelli, R.; Nahon, M. *Modeling and Control of a Tailsitter UAV*; IEEE: Piscataway, NJ, USA, 2018; pp. 400–409.
9. Lustosa, L.R.; Defaÿ, F.; Moschetta, J. Longitudinal study of a tilt-body vehicle: Modeling, control and stability analysis. In Proceedings of the International Conference on Unmanned Aircraft Systems (ICUAS), Denver, CO, USA, 9–12 June 2015; pp. 816–824.
10. Zhao, Q.; Zhou, Z.; Li, M.; Xu, D. Propulsion-aerodynamic coupling model of distributed power wing-induced wing surface. *Acta Aeronaut. Astronaut. Sin.* **2024**, *45*, 129252.

11. Chen, Y. Experimental Research On aircraft with Electric Distributed Power Layout. Master's Thesis, Nanjing University of Aeronautics and Astronautics, Nanjing, China, 2019.
12. Wang, C.; Zhou, Z.; Wang, R.; Wang, K. Longitudinal stability research of ducted vertical take-off and landing fixed-wing UAV. *J. Northwestern Polytech. Univ.* **2021**, *39*, 712–720. [CrossRef]
13. Rao, C.; Zhang, T.; Wei, C.; Liu, Y. A mechanism of the influence of propeller slipstream of a distributed electric aircraft. *Acta Aeronaut. Astronaut. Sin.* **2021**, *42*, 726387.
14. Tekinalp, O.; Unlu, T.; Yavrucuk, I. Simulation and Flight Control of a Tilt Duct UAV. In Proceedings of the AIAA Modeling & Simulation Technologies Conference, Keystone, CO, USA, 21–24 August 2006. [CrossRef]
15. Akici, F.; Leblebcolu, M.K. Control System Design of a Vertical Take-off and Landing Fixed-Wing UAV. *IFAC Pap.* **2016**, *49*, 267–272. [CrossRef]
16. Cetinsoy, E.; Dikyar, S.; Hancer, C.; Oner, K.; Sirimoglu, E.; Unel, M.; Aksit, M. Design and construction of a novel quad tilt-wing UAV. *Mechatronics* **2012**, *22*, 723–745. [CrossRef]
17. Muraoka, K. Transition flight of quad tilt wing VTOL UAV. In Proceedings of the Congress of the International Council of the Aeronautical Sciences, Brisbane, Australia, 23–28 September 2012.
18. Cook, J.W.; Gregory, I.M. A Robust Uniform Control Approach for VTOL Aircraft. In Proceedings of the 2021 Autonomous VTOL Technical Meeting and Electric VTOL Symposium, Virtual, 26–28 January 2021.
19. Raab, S.A.; Zhang, J.; Bhardwaj, P.; Holzapfel, F. Proposal of a Unified Control Strategy for Vertical Take-off and Landing Transition Aircraft Configurations. In Proceedings of the 2018 Applied Aerodynamics Conference, American Institute of Aeronautics and Astronautics, Atlanta, GA, USA, 25–29 June 2018. [CrossRef]
20. Colunga, G.R.F.; Lozano, R. Transition Flight Control of the Quad-Tilting Rotor Convertible MAV. In Proceedings of the 2013 International Conference on Unmanned Aircraft Systems (ICUAS), Atlanta, GA, USA, 28–31 May 2013. [CrossRef]
21. Li, M. Design of Landing Strategy and Control Law for a Tail-Sitter Coaxial Rotor Aircraft. Master's Thesis, Nanjing University of Aeronautics and Astronautics, Nanjing, China, 2019.
22. Jiang, W. Research on Attitude Control of Tilt-Wing Aircraft During Vertical Take-Off and Landing Stage. Master's Thesis, Nanchang Hangkong University, Nanchang, China, 2017.
23. Wu, M.; Qi, R. Application of dynamic matrix control in automatic landing of flying wing UAV. *Sci. Technol. Eng.* **2012**, *12*, 7655–7668.
24. Wang, G.; Wu, Z. Comprehensive research on overall scheme analysis and control strategy of vertical take-off and landing UAV. *Aircr. Des.* **2006**, *2006*, 25–30.
25. Zhang, J.; Guo, Z.; Wang, R.; Wu, L. Application of Total Energy Control on Vertical Take-off and Landing UAV. In Proceedings of the 2019 IEEE 3rd Advanced Information Management, Communicates, Electronic and Automation Control Conference (IMCEC), Chongqing, China, 11–13 October 2019; pp. 1554–1558.
26. Wen, J.; Chen, S.; Yang, A.; Wang, Y. Research on Vertical Take-off and Landing Control of New VTOL Aircraft Based on ADRC. In Proceedings of the 2021 36th Youth Academic Annual Conference of Chinese Association of Automation (YAC), Nanchang, China, 28–30 May 2021; pp. 1–6.
27. Hu, R.; Wang, Z.; Chen, Y.; Zhou, D.; Yang, D.; Gong, Z. Stability augmentation control of thrust-vectored V/STOL aircraft based on L1 adaptive control. *Acta Aeronaut. Astronaut. Sin.* **2023**, *44*, 727642.
28. Zhong, J.; Song, B. Hover position control of tail-sitter aircraft based on L1 adaptive law. *Syst. Eng. Electron.* **2018**, *40*, 2062–2070.
29. Li, Y.; Liu, X.; Li, J.; Li, G. Longitudinal control and characteristic analysis of ship landing based on L1 adaptive. *Comput. Meas. Control* **2018**, *26*, 120–124.

Disclaimer/Publisher's Note: The statements, opinions and data contained in all publications are solely those of the individual author(s) and contributor(s) and not of MDPI and/or the editor(s). MDPI and/or the editor(s) disclaim responsibility for any injury to people or property resulting from any ideas, methods, instructions or products referred to in the content.